Experimental studies of lattice dynamical properties in indium nitride

2004 J. Phys.: Condens. Matter 16 R381

(http://iopscience.iop.org/0953-8984/16/12/R01)

INSTITUTE OF PHYSICS PUBLISHING JOURNAL OF PHYSICS: CONDENSED MATTER

J. Phys.: Condens. Matter **16** (2004) R381–R414 PII: S0953-8984(04)71723-3

TOPICAL REVIEW

Experimental studies of lattice dynamical properties in indium nitride

Z G Qian[1], W Z Shen[1,3], H Ogawa[2] and Q X Guo[2]

[1] Laboratory of Condensed Matter Spectroscopy and Opto-Electronic Physics, Department of Physics, Shanghai Jiao Tong University, 1954 Hua Shan Road, Shanghai 200030, People's Republic of China
[2] Department of Electrical and Electronic Engineering, Faculty of Science and Engineering, Saga University, Saga 840-8502, Japan

E-mail: wzshen@sjtu.edu.cn

Received 10 November 2003, in final form 5 January 2004
Published 12 March 2004
Online at stacks.iop.org/JPhysCM/16/R381(DOI:10.1088/0953-8984/16/12/R01)

Abstract

We review recent experimental studies on the lattice dynamical properties of novel semiconductor InN thin films. Most of the experimental results are concerned with Raman scattering as well as infrared spectroscopic studies. The emphasis is on the structure of Brillouin zone centre (Γ point) phonons in InN (including both the wurtzite and zinc blende structures), coupling between the electron excitation (plasmon) and the longitudinal optical phonon, disorder-activated modes, temperature- and pressure-dependences of the lattice vibration modes, micro-Raman imaging, and the lattice vibration in nitride alloys, superlattices, quantum wells, and quantum dots, etc. This article also presents some prospects on Raman scattering studies in the related materials and structures.

Contents

[3] Author to whom any correspondence should be addressed.

1. Introduction

III-nitride semiconductors, such as GaN, AlN, InN and their ternary alloys, are promising materials for optoelectronic and microelectronic devices [1, 2]. InN is preferred for low-cost solar cells with high efficiency, optical coatings, and various types of sensors [1]. InN has received more attention from the properties of its alloys with GaN and AlN, which permit the fabrication of InGaAlN based shortest-wavelength semiconductor laser diodes [3, 4]. Moreover, InN has distinct advantages in high-frequency centimetre and millimetre wave devices, because the transport characteristics of InN are superior to those of GaN and GaAs [5]. Recent studies show that InN and other III-nitrides are promising materials for terahertz (THz) radiation generation [6–8]. InN has also been proved to be a good plasma filter material in thermophotovoltaic (TPV) systems [9]. However, the growth of InN is the most difficult among the III-nitrides because the equilibrium vapour pressure of nitrogen over InN is several orders higher than that of AlN and GaN, and accordingly the studies on InN are relatively fewer than those on GaN and AlN due to the low decomposition temperature of InN, the difficulties of growing bulk InN, and the lack of proper substrates, whose lattice constants and thermal expansion coefficients both match InN, for thin film growth. With the improvement of growth techniques in the past few years, InN thin films have been successfully deposited on sapphire (α-Al_2O_3), GaAs, GaP, Si and glass substrates by magnetron sputtering, metalorganic vapour phase epitaxy or chemical vapour phase deposition (MOVPE or MOCVD) and molecular beam epitaxy (MBE) [10–19]. However, some important optical and electrical properties of InN have not been fully understood, such as the band gap E_g; most experimental values including the early results [20] are about 1.9–2.0 eV, but recently, high-quality InN thin films grown by MBE [21, 22] and MOVPE [23] with band gaps of 0.7–1.1 eV have been reported. According to theoretic calculations, InN has excellent steady and transient electron transport properties and the cut-off frequency of an InN field effect transistor (FET) can be higher than 400 GHz [5], but electrical studies on InN are limited to dark current and Hall measurements.

Since the first Raman report of InN in 1996 by Kwon *et al* [24], lattice vibration (phonon) studies of InN have led to large quantities of theoretical and experimental results, which need to be summarized to correspond to the recent review work on GaN [25]. Raman scattering is a standard optical characterization technique for studying various aspects of solids such as lattice properties, electronic properties, and magnetic properties. Raman scattering has many advantages compared with other spectroscopic techniques: it is in principle non-destructive, contactless, and requires no special sample preparation technique such as thinning or polishing. On the other hand, nitride semiconductors are suitable for Raman scattering studies, since the chemical bonding is a mixture of covalent and ionic bonding, which has a relatively high phonon scattering efficiency, and they are generally robust and stand up well to laser irradiations.

InN has two possible structures: the hexagonal wurtzite and the cubic zinc blende (as shown in figure 1); table 1 shows some of their fundamental parameters [1, 5, 25, 26]. Since the wurtzite structure is the stable phase while the zinc blende structure is metastable, most of the present studies on InN concentrate on hexagonal wurtzite InN (h-InN). This article reviews lattice vibrational studies on h-InN, mainly emphasizing the phonon structure in the

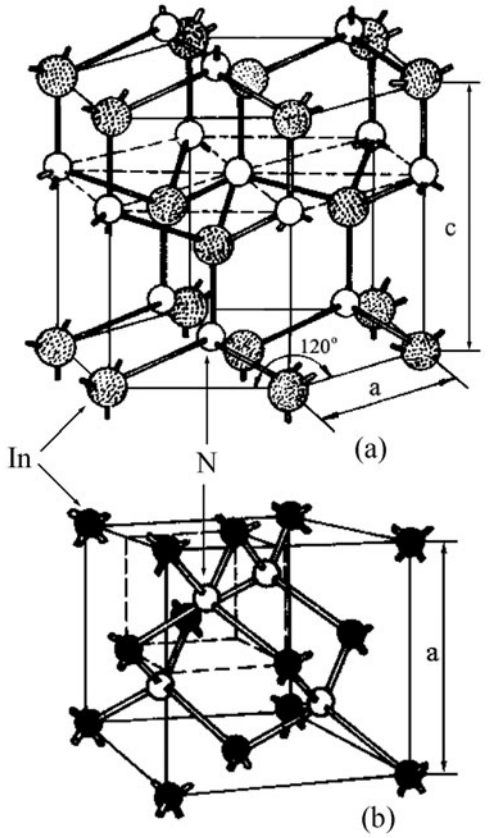

Figure 1. The structure of (a) wurtzite InN (h-InN) and (b) zinc blende InN (c-InN).

Brillouin zone centre (the Γ point), plasmon and longitudinal optical (LO) phonon (PLP) coupling modes, disorder-activated modes, micro-Raman and temperature and pressure effects of phonon modes. In addition, we also discuss the lattice vibration results of cubic zinc blende (c-InN), ternary alloys of InGaN and AlGaN, and the low-dimensional structures such as superlattice, quantum well and quantum dot structures.

The Raman scattering of phonons in crystals can be explained by the interactions of phonons and photons [27, 28]. An incident photon with frequency of ω_{L} interacts with the phonons in crystals and then annihilates or generates a phonon with frequency of ω_{ph}, so the frequency of the scattering photon is

$$\omega_{\mathrm{s}} = \omega_{\mathrm{L}} \pm \omega_{\mathrm{ph}}. \tag{1}$$

As regards the wavevectors of the incident photon k_{L}, phonon $\mathbf{q}$ and scattering photon k_{s}, they are related by

$$k_{\mathrm{s}} = k_{\mathrm{L}} \pm q. \tag{2}$$

Equations (1) and (2) correspond to energy conversation and momentum conservation, respectively. The scattering is called Stokes scattering if the '−' condition is satisfied and anti-Stokes scattering if the '+' condition is satisfied. The frequency shift of the scattering photon is called Raman shift, which corresponds to the phonon frequency and is generally in the range of 50–1000 cm^{-1}. Lasers from near-infrared to near-ultraviolet ($k_{\mathrm{L}} \approx 10^6\ \mathrm{cm}^{-1}$) are generally employed in experiments; the maximum of the wavevector change during the

Table 1. Some fundamental parameters of InN.

Structure	Parameters	Values	Units
Hexagonal wurtzite h-InN	Mass density	6.81	g cm^{-3}
	Band gap E_g (300 K)	1.89[a]	eV
	Temperature coefficient dE_g/dT	−1.8	10^{-4} eV K^{-1}
	Pressure coefficient dE_g/dP[b]	19	meV GPa^{-1}
	Lattice constants	$a = 3.54$	Å
		$c = 5.70$	Å
	Thermal expansion coefficient	$\Delta a/a \sim 4$	10^{-6} K^{-1}
		$\Delta c/c \sim 3$	10^{-6} K^{-1}
	Deformation potential	7.1	eV
	Longitudinal sound velocity	6.24	10^5 cm s^{-1}
	Transverse sound velocity	2.55	10^5 cm s^{-1}
	Piezoelectric coefficient	3.75	10^{-5} C cm^{-2}
	Thermal conductivity	0.8	W cm^{-1} K^{-1}
	Dielectric constants[c]	$\varepsilon_\infty = 8.4$	
		$\varepsilon_{r0} = 15.3$	
	Effective mass of electron[c]	0.115	m_0
	Electron saturating velocity	2.5	10^7 cm s^{-1}
Cubic zinc blende c-InN	Band gap E_g (300 K)	2.2	eV
	Pressure coefficient dE_g/dP[b]	22	meV GPa^{-1}
	Lattice constants[a]	4.98	Å
	Dielectric constants[b]	$\varepsilon_\infty = 8.9$	
		$\varepsilon_{r0} = 10.2$	

[a] Recently, much lower band gaps of 0.7–1.1 eV have been observed in MBE [21, 22] and MOVPE [23] grown InN thin films.
[b] Theoretical calculations.
[c] Average values.

scattering (i.e., the wavevector of the phonon) is $2k_L$, which is much smaller than the Brillouin zone. We can therefore conclude that only the phonons near the Brillouin zone centre (Γ point) will contribute to the Raman scattering by equation (2). Studies of other critical points are usually carried out by x-ray diffraction and neutron scattering measurements. The geometry configuration used to describe the Raman scattering experiments is normally described as $k_L(a_L, a_s)k_s$ = incident direction (incident polarization, scattering polarization) scattering direction. The Raman scattering section can be written as

$$\frac{d\sigma}{d\Omega} = W|a_s \cdot \vec{R} \cdot a_L|^2 \tag{3}$$

where W is a constant and $\vec{R}$ is the Raman tensor, which is related to the polarizability tensor $\vec{\chi}_{ij}$ of the crystal:

$$R_{ij}^{\mu} = \left.\frac{\partial \vec{\chi}_{ij}}{\partial Q^{\mu}}\right|_{Q_0^{\mu}} \Delta Q_0^{\mu}. \tag{4}$$

For one lattice vibrational mode, it can be observed in the Raman spectrum only if the experiment is under the geometry configuration when the scattering section does not equal zero, which is called the group theory selection rules. It is called first-order Raman scattering when the scattering process involves only one phonon, and multi-order scattering when it involves more than one phonon. Generally, we can observe second-order scattering in experiments, i.e., annihilate or generate two phonons at the same time or annihilate one phonon and generate

another one. In this case, the phonons that contribute to the Raman scattering can be other than the Γ point ones, so long as they satisfy equations (1) and (2).

Infrared (IR) reflection and transmission are also frequently employed to study lattice vibrations [27]. In normal incident configuration, we can obtain the dielectric constant spectra and the corresponding optical constant spectra from the reflection spectra by the Kramers–Kronig (KK) transformation, and then the phonon frequencies can be determined by their extreme values. Another method is to use the fundamental Fresnel formula to calculate the reflection spectra after considering the reflections and transmissions at interfaces, with the contributions of transverse optical (TO) phonons and free carriers to the dielectric function by the multi-oscillator model and the Drude model, respectively. By fitting the experimental reflection spectra, we can obtain the phonon frequency, oscillator strength and damping constant, which had been successfully applied in studying the phonon characteristics of GaN [29]. However, IR reflection studies are relatively fewer compared with Raman studies since they are not as direct as Raman scattering, and there has so far been no IR transmission study reported, because of the experimental difficulties. Infrared spectroscopic ellipsometry (IRSE) is another way to obtain the optical constants from the measured amplitude attenuation and phase shift without the KK transformation.

2. Lattice vibrations of wurtzite InN

2.1. Theoretical calculations

Wurtzite InN (h-InN; see figure 1(a)) has four atoms per unit cell, i.e., two In–N atom pairs. Zinc blende InN (c-InN; see figure 1(b)) has two atoms per unit cell, i.e., one In–N atom pair. In both cases, one In atom is involved in an N atom tetrahedron and vice versa. h-InN is different from c-InN only in the stacking order of In–N atom layers: h-InN is ABAB... type along the [0001] direction and c-InN is ABCABC... type along the [111] direction. The phonon structure of h-InN is relative to that of c-InN, i.e., the phonon dispersion along [0001] ($\Gamma \rightarrow$ A direction in Brillouin zone) in h-InN can be approximately obtained by folding the phonon dispersion along [111] ($\Gamma \rightarrow$ L direction) in c-InN.

h-InN belongs to the C_{6v}^4 space group. Group theory predicts one A_1, one E_1, two E_2 and two B_1 modes and the corresponding polarization tensors can be written as follows:

$$A_1(z) = \begin{vmatrix} a & 0 & 0 \\ 0 & a & 0 \\ 0 & 0 & b \end{vmatrix} \qquad E_1(x) = \begin{vmatrix} 0 & 0 & c \\ 0 & 0 & 0 \\ c & 0 & 0 \end{vmatrix} \qquad E_1(y) = \begin{vmatrix} 0 & 0 & 0 \\ 0 & 0 & c \\ 0 & c & 0 \end{vmatrix}$$
$$E_2 = \begin{vmatrix} d & d & 0 \\ d & -d & 0 \\ 0 & 0 & b \end{vmatrix} \qquad B_1 = \begin{vmatrix} e & f & 0 \\ f & -e & 0 \\ 0 & 0 & 0 \end{vmatrix}. \tag{5}$$

A_1 and E_1 symmetry are modes corresponding to the axial and planar vibrations, respectively. They split into longitudinal acoustic and optical (LA and LO) and transverse acoustic and optical (TA and TO), and the LO and TO branches can be activated both in Raman and infrared spectra. E_2 and B_1 are non-polar modes and E_2 is only Raman active while the B_1 mode is forbidden. Figure 2 gives the vibrational types of the atoms in the unit cell corresponding to these phonon modes, and E_2 and B_1 each have two modes marked '(high)' and '(low)' according to their frequencies. Therefore, the Raman active modes of h-InN are A_1 (LO), A_1 (TO), E_1 (LO), E_1 (TO), E_2 (high) and E_2 (low). Table 2 shows the observable modes in different geometry configurations based on group theory selection rules. Several groups have calculated the phonon dispersion and phonon density of states (DOS) [30–37]. Figure 3 shows one of the calculated phonon dispersion and DOS results [31]. We can see

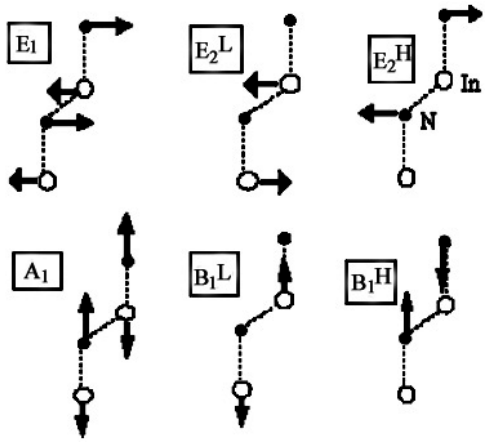

Figure 2. The atom vibration modes in h-InN with the c axis upwards. The superscripts H and L represent the high and low frequency modes, respectively.

Table 2. Active phonon modes in h-InN at different geometry configurations (the z direction is defined parallel to the c axis of h-InN).

Geometry configurations	Active phonon modes
$x(y, y)\overline{x}$	A_1 (TO), E_2
$x(z, z)\overline{x}$	A_1 (TO)
$x(z, y)\overline{x}$	E_1 (TO)
$x(y, z)y$	E_1 (TO), E_1 (LO)
$x(y, y)z$	E_2
$z(x, y)\overline{z}$	E_2
$z(x, x)\overline{z}$	A_1 (LO), E_2

from figure 3 that most optical phonons at the Γ point are in the range of 400–600 cm^{-1} except that E_2 (low) and B_1 (low) are about 100 and 200 cm^{-1} and the LO–TO splitting of A_1 is larger than that of E_1. Furthermore, we can see four peaks from the DOS located at 100, 200, 490 and 570 cm^{-1}, respectively, which agree well with the disorder-activated Raman spectrum from N^+ ion implanted h-InN shown in figure 3(c). This similarity will be discussed in section 2.4.

2.2. Raman scattering experiments

From the selection rules and table 2, A_1 (LO) and E_2 modes can be observed in back scattering $z(x, -)\overline{z}$ configuration, which is widely employed since nearly all studies have been made on films grown with the c-axis normal to the substrate surface. The z direction is defined parallel to the c axis of h-InN. When we take the polarization into account, both A_1 (LO) and E_2 can be observed at $z(x, x)\overline{z}$, while only E_2 can be observed at $z(x, y)\overline{z}$ and the non-back scattering configurations should be taken in order to observe other phonon modes. Figure 4 shows the earliest Raman spectra of h-InN thin films, which were deposited on sapphire substrates by MOVPE [24]. We can see that the relative intensities of A_1 (LO) and E_2 (high) at different configurations agree well with the selection rules.

In fact, the deposited InN thin films are not ideal crystals, so the selection rules will relax, which will result in the observation of the non-activated modes. For example, figure 5 gives the Raman spectra of an InN thin film, which was deposited by atomic layer epitaxy (ALE) on sapphire substrates [38]. We can observe six modes at the back scattering configuration of $z(x, x)\overline{z}$, even the forbidden B_1 mode. Table 3 gives typical Raman scattering and theoretical

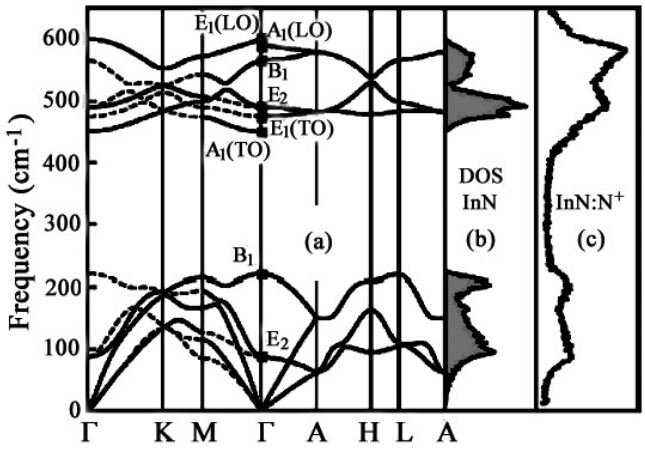

Figure 3. h-InN (a) phonon dispersion curves, (b) phonon density of states (DOS) and (c) DA Raman spectrum at low temperature (7 K) after N^+ implantation (from [31]).

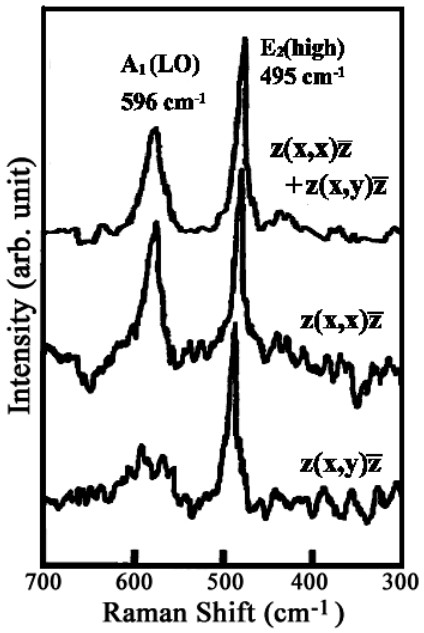

Figure 4. Raman scattering spectra of h-InN thin film at different geometry configurations. The relative intensity of A_1 (LO) and E_2 corresponds to group theory selection rules (from [24]).

calculation results available in the literature. Although the phonon structure at the Γ point is fairly clear, there are differences as large as 10 cm^{-1} between the reported results. This is mainly caused by the material diversity and the disorder activation, stress and temperature effects etc, which will be discussed in sections 2.4 and 2.5.

In addition, Kaczmarczyk *et al* observed second-order Raman scattering of an h-InN thin film (see figure 6) [32]. The InN thin film was grown by MBE on GaN (0001) substrates with a thickness of 120 nm, and the spectrum was excited by a 488 nm laser. In the low frequency region, 145 cm^{-1} is the acoustic phonon at the A point, 205 cm^{-1} is the overtone of the TA phonon at the K or M point, and the authors also pointed out that the structure at about 200 cm^{-1} observed by Inushima *et al* [38] is also second-order scattering, rather than the forbidden B_1

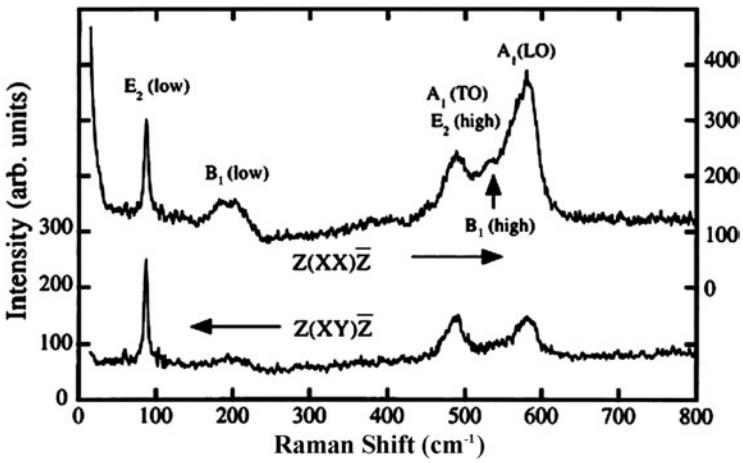

Figure 5. Raman spectra of h-InN thin film. Six optical modes can be observed due to the relaxation of the selection rules (from [38]).

Table 3. The typical calculated (Cal.) and experimental (Exp.) phonon frequencies (in cm^{-1}) of h-InN in the literature.

Phonon modes	E_2 (low)	B_1 (low)	A_1 (TO)	E_1 (TO)	E_2 (high)	B_1 (high)	A_1 (LO)	E_1 (LO)
[24] Exp.					495		596	
[38] Exp.	87	200	480		488	540	580	
[31] Exp.	87		447	476	488		586	593
[33] Cal.	83	225	443	467	483	576	586	595
[39] Exp.			445	472	488		588	
Cal.	104	270	440	472	483	530		
[16] Exp.			441–445	471–475	489–491		588–591	
[32] Exp.	88		440		490		590	
[35] Cal.	93	202	443	470	492	568	589	605
Cal.	85	217	449	457	485	566	587	596

(low) mode. In the high frequency region, 678 cm^{-1} is the A_1 (LO) + A_1 (LA) mode at the K or M point and 850–1200 cm^{-1} are the resonant frequencies of optical modes.

2.3. Plasmon and LO phonon coupling mode

The excited states of free electrons in semiconductors can also contribute to Raman scattering. Here we discuss the collective excited mode, i.e., the plasmon, whose dispersion relation can be written as [27]

$$\omega_p^2(q) = \omega_p^2 + \tfrac{3}{5}q^2 v_F^2 \tag{6}$$

where q is the wavevector of plasmon, and ω_p is the plasmon frequency when $q = 0$:

$$\omega_p^2 = n_e e^2/(\varepsilon_0 \varepsilon_\infty m_e^*) \tag{7}$$

where n_e is the electron concentration, ε_0 is the vacuum dielectric constant, ε_∞ is the relative high frequency dielectric constant and m_e^* is the effective mass of electron. V_F is the Fermi velocity which corresponds to the Fermi energy $E_F = \hbar\omega_F = \hbar^2 k_F^2/2m_e^*$ and

$$v_F = \hbar k_F/m_e^* \tag{8}$$

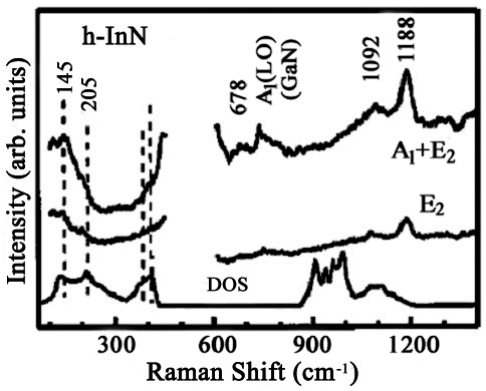

Figure 6. Second-order Raman scattering structures of h-InN excited by a 488 nm laser. The scattering configurations are $A_1 + E_2[z(x, x)\bar{z}]$ and $E_2[z(x, y)\bar{z}]$ (from [32]).

with k_F the Fermi wavevector, and when $T = 0$ K

$$k_F = (3\pi^2 n_e)^{1/3}. \tag{9}$$

Since almost all the InN thin films obtained so far are n type with high electron concentration ($>10^{18}$ cm^{-3}), i.e., ω_p is relatively large, the coupling of the plasmon and the LO phonon (PLP) will be enhanced to form the PLP coupling mode. The coupling mode splits into two branches, the upper (PLP$^+$) and the low (PLP$^-$) branch. When $q = 0$, their frequencies can be described by

$$\omega^2_{\pm,i} = \tfrac{1}{2}(\omega^2_{p,i} + \omega^2_{LO,i}) \pm \tfrac{1}{2}[(\omega^2_{LO,i} + \omega^2_{p,i})^2 - 4\omega^2_{p,i}\omega^2_{TO,i}]^{1/2} \tag{10}$$

where $\omega^2_{p,i} = n_e e^2/(\varepsilon_0 \varepsilon_{\infty,i} m^*_{e,i})$ and $i =$ '$\parallel$' or '$\perp$'. With increasing ω_p, the PLP$^+$ increases from the LO frequency to high frequency and the PLP$^-$ approaches the TO frequency. It should be noted that most observed PLP modes so far are PLP$^-$ [14, 21, 23, 31]. Figure 7(a) shows the Raman spectra of Mg doped InN from Davydov *et al* [31]. We can observe, with increasing carrier concentration, the PLP$^-(\parallel)$ mode approaches the A_1 (TO) frequency ($\sim$450 cm^{-1}). Figure 7(b) shows the corresponding IR reflection spectra (related to the E_1 symmetry modes) and the plasma reflection edges, from which the value of ω_p can be estimated, displaying the same tendency, which will be discussed in section 2.8. Figure 8 shows the relationship between the PLP frequencies and the electron concentration, and we can see that the Raman scattering results [14, 21, 31] agree well with the calculations from equations (7) and (10).

It should be pointed out that electrons with high concentration will screen the LO phonon, but the A_1 (LO) mode can still be observed in Raman spectra in addition to the PLP modes. The reason is not yet clear, and one possible explanation is that the A_1 (LO) mode originates from the depletion layer [39]. Nevertheless, Kasic *et al* [40] excluded the existence of the depletion layer and attributed the observed A_1 (LO) mode to the PLP coupling mode with large wavevector, because when $q > q_c \approx m^*_e\omega_p/\hbar k_F$, the collective excited mode would degenerate to one-particle mode (i.e., enter into the Landu damping area) [41] and PLP$^-$ approaches the unscreened A_1 (LO) frequency.

2.4. Disorder activated mode

Disorder-activated (DA) modes are caused by the breakdown of the translational symmetry in the disordered lattice; thus the phonons at Brillouin zone edges can also contribute to first-order Raman scattering. In this case, the Raman spectra should reflect the features of the DOS, for instance as observed in the heavily Mn doped GaN [42] and InN:N$^+$ shown in figure 3(c), where the low temperature (7 K) Raman spectrum of the N$^+$ implanted InN thin film is very

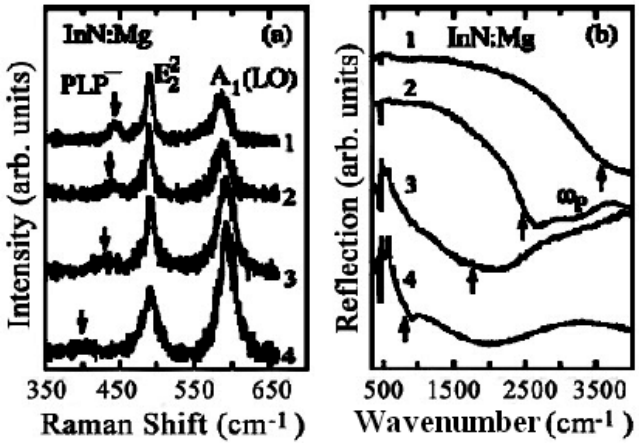

Figure 7. (a) Raman spectra and (b) IR reflection spectra of Mg doped InN thin films. The carrier concentrations of samples no 1, 2, 3 and 4 are 2×10^{20}, 1×10^{20}, 5×10^{19} and 1×10^{19} cm^{-3}, respectively (from [31]).

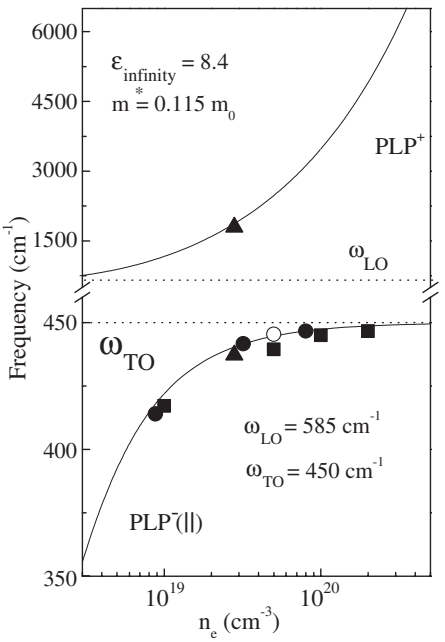

Figure 8. The dependence of PLP coupling mode frequencies on electron concentration (n_e). The solid curves are the calculated results, the filled circles, open circles and squares are Raman results from [14, 21, 31], and the triangles are from the ellipsometry results in [40].

similar to the calculated DOS curve. In fact, the inevitably existing defects, such as nitrogen vacancies and dislocations, will somehow result in disorder activation.

The disorder activated lattice vibrations can be quantitatively explained by the spatial correlation model (SCM), which was used to describe the Raman spectra of alloy semiconductors [43] and nano-silicon [44, 45]. This model assumes that the phonon can freely propagate in an area with a size of L (correlation length) and would be scattered with the phonon beyond this area. From the SCM, the Raman scattering intensity can be written as

$$I(\omega) \simeq \int_0^1 \frac{\exp(-q^2L^2/4a^2)\,\mathrm{d}^3q}{[\omega - \omega(q)]^2 + (\Gamma_0/2)^2} \tag{11}$$

where the wavevector q is in units of $2\pi/a$, a is the lattice constant, L is the correlation length (Å), Γ_0 is the scattering peak width in an ideal lattice, $\omega(q)$ is the dispersion relationship of phonon, and the integration is taken over a spherical Brillouin zone, i.e., the dispersion relation is taken as isotropic. Various one-dimensional approximations of $\omega(q)$, taking the forms [43, 46, 47] of

$$\omega^2(q) = A + \{A^2 - B[1 - \cos(\pi q)]\}^{1/2} \tag{12a}$$

$$\omega(q) = [A + B\cos(\pi q/2)]^{1/2} \tag{12b}$$

or

$$\omega(q) = A + B\cos(\pi q) \tag{12c}$$

where A and B are constants determined by experiments, have been used.

As figure 9 shows [48], the Raman scattering structures of InN thin films grown by different methods are quite different. Compared with the InN thin film grown by MOVPE, the magnetron sputtered one has a relatively poor crystalline quality, which means a high defect density and a strong DA effect. We can see that the LO-like structure (i.e., the DALO) has a manifest red shift, broadening and asymmetry. Furthermore, an additional band similar to the LA structure in DOS (i.e., the DALA) emerges in the low frequency region. Similar structures have also been reported in several references, such as the InN thin film deposited at low temperature by MOVPE [49, 50], randomly oriented polycrystalline InN [39], InN thin film with high growth rate by MOCVD [51] and InN nano-wire [52] etc; we attribute these structures to the DA phonon modes.

Recently, Qian *et al* [53] studied the DA Raman scattering of InN thin films sputtered on GaAs substrates at low temperature (100 °C) and quantitatively explained the experimental results with SCM. Figure 10 shows the fitting results of the DA Raman scattering of two InN thin film samples sputtered at different pressures (the contributions from GaAs substrates have been subtracted). A good fit can be obtained by a combination of SCM and a Lorentz line for the DALO peak. We can also obtain a series of parameters, such as the correlation length L, frequency shift of peak position $\Delta\omega$ and the asymmetry parameter Γ_a/Γ_b etc. The Lorentz peak at about 490 cm^{-1} was usually attributed to the Brillouin zone edge phonon in some cases [54, 55], and its relative intensity to the SCM peak will increase when L decreases. But here the fitting results give the opposite tendency, and the value corresponds to the E_2 (high) frequency; this Lorentz peak is therefore attributed to the DA E_2 (high) mode. The DA mode does not have a large red shift because the E_2 (high) mode has a relatively flat dispersion relation. This study links the correlation length L to the growth conditions of InN thin films and L can be physically explained as the average distance between the defects, which reflects the crystalline quality. As a result, we can investigate the effects of growth conditions on the structure and quality of InN thin films. Pan *et al* [56] studied the influences of the nitriding conditions of sapphire substrates. As figure 11 shows, we can estimate the thin film quality from the Raman peak width, in order to select the optimizing nitriding condition. For GaN, there have been detailed studies on this topic [57].

2.5. Temperature and stress effects

Generally, when the temperature (T) increases, the phonon frequency $\omega(T)$ decreases and the peak width broadens. This frequency shift $\Delta\omega(T)$ can be divided into two additive parts: one is due to the lattice thermal expansion $\Delta\omega_1(T)$ and the other is due to the anharmonic coupling with other phonons. They can be written as [58, 59]

$$\Delta\omega(T) = \omega(T) - \omega_0 = \Delta\omega_1(T) + \Delta\omega_2(T) \tag{13}$$

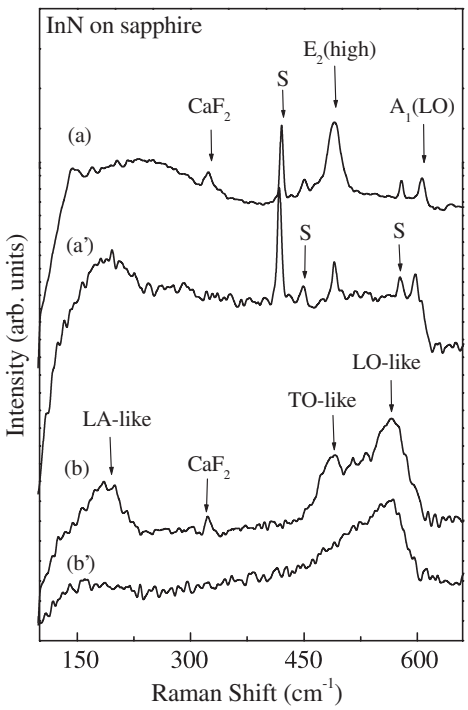

Figure 9. Raman spectra of InN thin films deposited on sapphire substrates grown by MOVPE and measured at (a) 77 K and (a′) room temperature; magnetron sputtering and measured at (b) 77 K and (b′) room temperature. The peaks marked with 'S' are from the sapphire substrate and 'CaF_2' from the window of the Dewar (from [48]).

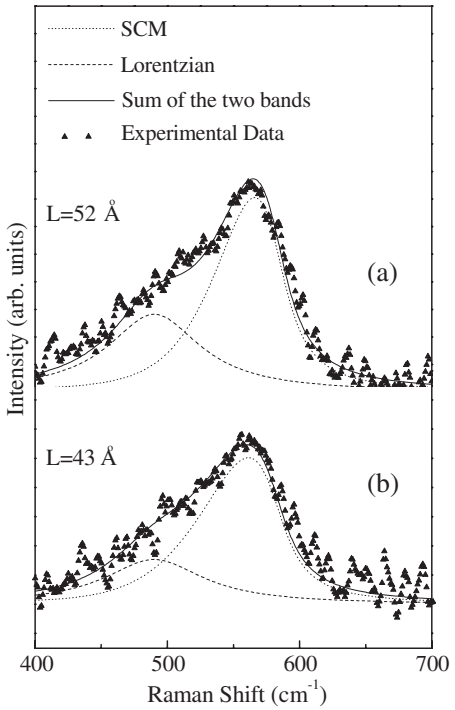

Figure 10. DA Raman scattering spectra and the fitting results of InN thin films deposited on GaAs substrates. The samples are sputtered at 100 °C with a sputtering pressure of (a) 10 mTorr and (b) 1 mTorr (from [53]).

where ω_0 is the harmonic frequency of the phonon and

$$\Delta\omega_1(T) = -\omega_0\gamma \int_0^T [\alpha_c(\tilde{T}) + 2\alpha_a(\tilde{T})]\,\mathrm{d}\tilde{T} \tag{14}$$

$$\Delta\omega_2(T) = A'[1 + 2n(T, \omega_0/2)] + B'[1 + 3n(T, \omega_0/3) + 3n^2(T, \omega_0/3)] \tag{15}$$

where α_c and α_a are temperature dependent linear expansion coefficients parallel and perpendicular to the c axis of the hexagonal wurtzite structure, γ is the Grüneisen coefficient, A' and B' are constants, and $n(T, \omega) = [\exp(\hbar\omega/k_B T) - 1]^{-1}$ is the Bose–Einstein distribution. The scattering peak width is

$$\Gamma(T) = \Gamma_0' + C[1 + 2n(T, \omega_0/2)] + D[1 + 3n(T, \omega_0/3) + 3n^2(T, \omega_0/3)] \tag{16}$$

where C and D are constants and Γ_0' represents the contributions from the defect and impurity scattering.

Detailed studies on the temperature effect of Raman scattering for GaN and AlN have been reported [58–60]. For InN, figure 9 gives the Raman spectra at room temperature and 77 K of two InN thin film samples [48]. For MOVPE grown InN thin film, the A_1 (LO) and E_2 (high) peaks shift from 490, 598 cm^{-1} at room temperature to 491, 607 cm^{-1} at 77 K. The magnetron sputtering InN thin film also has evident temperature effects. There is only an LO-like (DALO) scattering band centred at 570 cm^{-1} at room temperature, while an evident

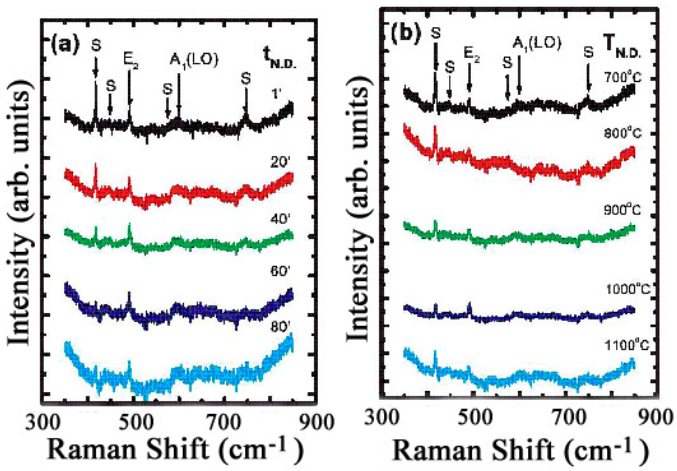

Figure 11. Raman spectra of InN on sapphire substrate, with the nitriding conditions of (a) 1000 °C and different times (1–80 min) and (b) 40 min and different temperatures (700–1100 °C) (from [56]). (This figure is in colour only in the electronic version)

TO-like scattering band emerges and the DALA band centred at about 200 cm^{-1} becomes clearer. There is no detailed report about the temperature effect of Raman scattering in InN, which needs more detailed temperature dependent Raman experimental data.

The stress effect (i.e., the phonon frequency shift due to the stress) of phonon modes has been reported in detail for GaN and AlN [61–65]. Kozawa *et al* [63] pointed out that at biaxial stress, the relation between the frequency shift $\Delta\omega$ of E_2 mode and the stress σ is

$$\Delta\omega = 6.2\sigma \tag{17}$$

where the stress is in units of GPa. We can use the Grüneisen coefficient γ to describe the relation between the lattice thermal expansion and the frequency shift:

$$\gamma_i = \frac{B_0}{\omega_i}\frac{d\omega_i}{dP}\bigg|_{P=0} \tag{18}$$

where ω_i is the frequency of the ith phonon, P is the hydrostatic pressure, and B_0 is the bulk elastic modulus, whose relation with elastic constants C_{ij} is [66]

$$B_0 = \frac{(C_{11}+C_{12})C_{33}-2C_{12}^2}{C_{11}+C_{12}+2C_{33}-4C_{13}}. \tag{19}$$

We can see that this description corresponds well to the temperature effect of equation (14). The deformation potential constant can also be used to describe the stress effect. When the stress is uniaxial and parallel to the c axis or biaxial and perpendicular to the c axis, the strain tensor ε_{ij} satisfies $\varepsilon_{xy} = \varepsilon_{yz} = \varepsilon_{zx} = 0$ and $\varepsilon_{xx} = \varepsilon_{yy}$. The frequency shift is

$$\Delta\omega = 2\alpha\varepsilon_{xx} + \beta\varepsilon_{zz} = 2\tilde{\alpha}\sigma_{xx} + \tilde{\beta}\sigma_{zz} \tag{20}$$

where α, β (in cm^{-1}) and $\tilde{\alpha}$, $\tilde{\beta}$ (in cm^{-1} GPa^{-1}) are deformation potential constants, and σ_{ij} is the stress tensor. When the stress is biaxial and the strain is elastic, we have $\sigma_{zz} = 0$ and

$$\sigma_{xx} = \sigma_{yy} = G_{ab}\varepsilon_{xx} \tag{21}$$

where G_{ab} is the biaxial elastic modulus, which can be calculated from the elastic constants:

$$G_{ab} = C_{11} + C_{12} - \frac{2C_{13}^2}{C_{33}}. \tag{22}$$

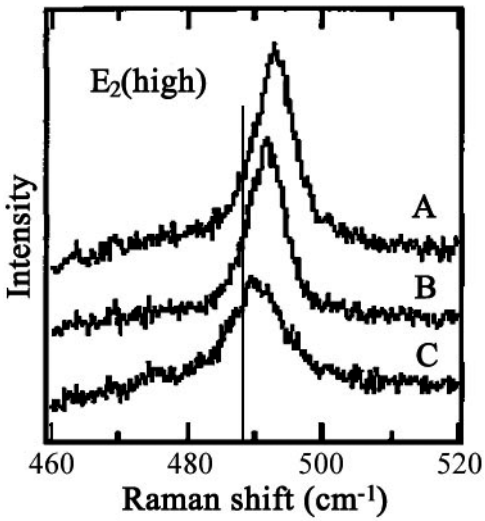

Figure 12. E_2 (high) modes of InN thin films grown at different temperatures: A, B and C correspond to 650, 600 and 500 °C, respectively. The line position at 488 cm^{-1} is the reported value in [38] grown at 440 °C (from [71]).

Generally, there are thermal residual strains in thin films, which are due to the different expansion coefficients between the thin film and the substrate when the thin film is cooling down after a high temperature growth. When the growth is along the *c* axis, the residual strain is biaxial and perpendicular to *c* axis, and can be estimated by

$$\varepsilon_{xx} = (T_g - T_r)(\alpha_{sub} - \alpha_{film}) \tag{23}$$

where T_g and T_r are growth temperature and room temperature, and α_{sub} and α_{film} are expansion coefficients (along the *a* axis of the wurtzite structure) of the substrate and thin film, respectively. For the InN thin film and sapphire substrate, α_{sub} and α_{film} are 7.5×10^{-6} and 4.0×10^{-6} K^{-1}, and during the cooling process, there will be a compressive stress in the thin film because the expansion coefficient of the substrate is larger. If the reliable stress effect parameters (Grüneisen coefficient or deformation potential coefficient) can be obtained experimentally, we can monitor the stress status in thin films by Raman scattering.

The influences of stress effects have been noticed in earlier studies. For example, [16] mentioned that the Raman peak positions shift 3–4 cm^{-1} for InN thin films deposited by MBE on Si(111) substrates at different temperatures (450–550 °C). There are both experimentally and theoretically reported elastic constants of InN thin films [67–70] for quantitative studies of the stress effect. Qian *et al* [48] estimated G_{ab} to be 239 GPa and obtained the stress effect of the A_1 (LO) mode in InN thin film grown on sapphire by MOVPE as $\Delta\omega = 23.9\sigma_{xx}$. Kurimoto *et al* [71] studied InN thin films grown by MOCVD and obtained the relation between the frequencies of E_2 (high) mode and the residual strain (%): $\omega = 50\varepsilon_{xx} + 481.5$ (cm^{-1}). Figure 12 clearly shows that when the growth temperature increases, the E_2 (high) peak shifts to higher frequencies.

2.6. Micro-Raman imaging

Micro-Raman imaging has become an important technology for studying spatial fluctuations. When excited by a visible laser, the lateral resolution can reach 1 μm or even higher; this can be used to study the distributions of strain, carrier concentration, polytype (cubic or

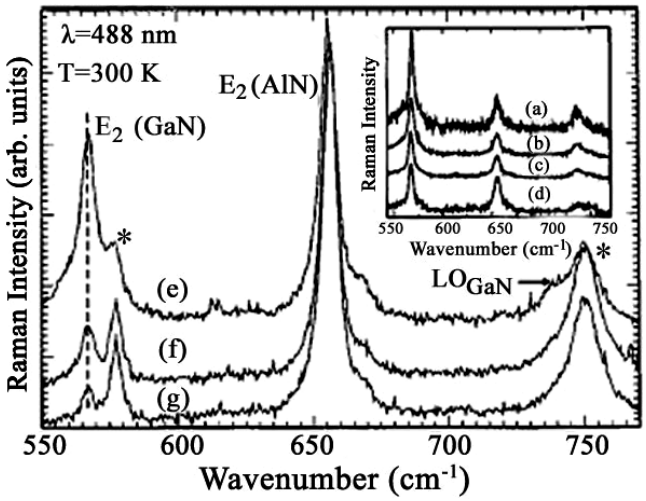

Figure 13. Micro-Raman spectra from an individual GaN pillar of (a) 5 μm, (b) 2 μm, (c) 1 μm, and (d) 600 nm diameter (inset), and of (e) 400 nm, (f) 200 nm, and (g) 100 nm diameter. Asterisks indicate sapphire structure Raman bands (from [72]).

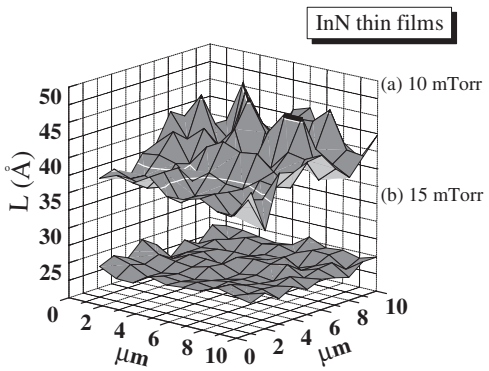

Figure 14. Distribution of the correlation length L in InN thin films with sputtering pressures of 10 and 15 mTorr, respectively. The scanning area is 9 μm $\times$ 9 μm with a spatial resolution of 1 μm (from [73]).

hexagonal) and lattice defects in nitride semiconductors. Some studies on GaN in this area have been summarized in [25]. Furthermore, the combination of a high spatial resolution optical technique and surface structuration opens up a detailed investigation into nano/micrometre-size fine patterning nitride objects for high performance electronic and optoelectronic devices. Demangeot *et al* [72] studied the micro-Raman and micro-photoluminescence (PL) properties of GaN pillars fabricated by electron beam lithography and reactive ion etching (RIE) on top of an AlN buffer layer. Figure 13 displays a set of Raman spectra for GaN pillars of different sizes from 5 μm to 100 nm in diameter. In addition to the clear decrease of the intensity of the GaN E_2 phonon (at 568 cm^{-1}) with respect to the AlN E_2 phonon when decreasing the GaN pillar size, the frequency red shifts of the E_2 mode indicate a partial relaxation of the strain in the GaN pillars. Micro-PL mapping gives strong evidence for defect induced donors and/or acceptors near the facets of the RIE etched pillars.

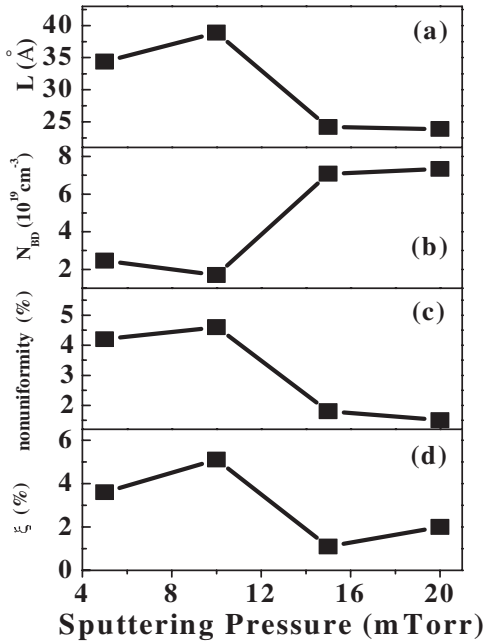

Figure 15. Dependence of (a) the average correlation length L, (b) the trap concentration N_{BD}, (c) the nonuniformity of the correlation length, and (d) the fractional variation ξ of the correlation lengths on the sputtering pressure in InN thin films grown by reactive sputtering at 100 °C (from [73]).

For InN, the micro-Raman study is currently at an early stage. Recently, Chen *et al* [73] have carried out detailed micro-Raman mappings on hexagonal InN thin films grown by reactive sputtering on GaAs(111) substrates at 100 °C under different sputtering pressures. Figure 14 shows the distribution of the calculated correlation length L after SCM fitting [53] over the surface mapping area of the InN thin films grown with pressures of 10 and 15 mTorr, respectively. It is clear that the sample under 10 mTorr pressure has larger L values, but the correlation length values fluctuate more severely than those in the 15 mTorr sample. Figure 15 shows the dependence of the average correlation length L, the trap concentration N_{BD}, the nonuniformity of the correlation length, and the fractional variation ξ of the correlation lengths on the sputtering pressure. It is found that the best average quality obtained for the 10 mTorr sample is at the expense of the sample's uniformity. The results have been discussed on the basis of growth mechanisms and roles of the grain size fluctuation in InN thin films: the crystalline 10 mTorr thin film, consisting of the largest crystalline grains, will show the best average quality. However, the size difference among the large grains will also be large, resulting in the high correlation length fluctuation. In contrast, the nearly amorphous 15 and 20 mTorr samples have almost no crystalline grains, and will definitely be more uniform.

Furthermore, the different grain size fluctuation induced nonuniformity in InN thin films will also have different effects in the InN/GaAs interfaces. In order to examine the InN/GaAs interface effects, Chen *et al* [73] have also performed Raman measurements with different laser wavelengths (figure 16) under the same backscattering geometry. When excited by a 1064 nm laser, the scattering signals are mainly from the GaAs substrate, and we can obtain the DA scattering structure as discussed in [53] after subtracting these substrate signals. The reason is that 1064 nm (1.17 eV) photon energy is below the band gap of this InN thin film

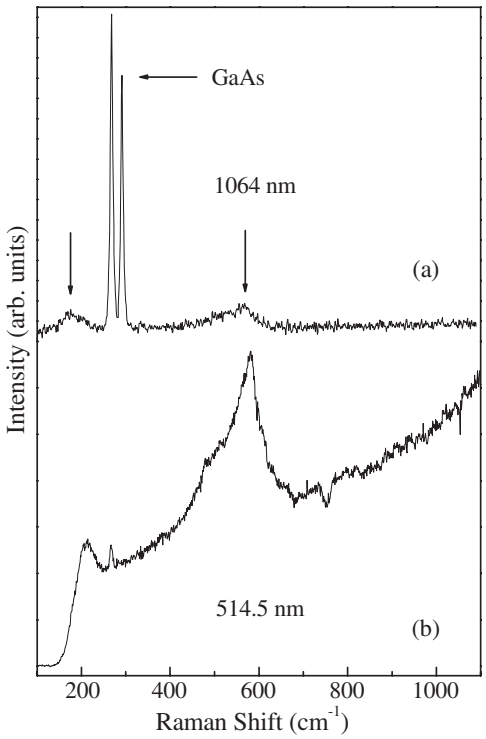

Figure 16. Raman spectra of one InN thin film sputtered on a GaAs(111) substrate excited by (a) 1064 nm and (b) 514.5 nm lasers.

(∼1.9 eV [74]), so the laser can penetrate the whole thin film layer (∼2 μm) and the scatterings from the substrate make a dominant contribution to the spectrum. In contrast, the 514.5 nm (2.41 eV) laser has a very small penetration depth because the photon energy is larger than the band gap and the absorption coefficient is very high. The interface influence on the InN thin film can be estimated by comparing the fractional variation ξ (figure 15(d)) between the SCM calculated correlation lengths from the wavelength dependent Raman spectra. It is found that ξ has exactly the same behaviour as the relative deviation (nonuniformity), clearly demonstrating the relationship between the grain size fluctuation (material nonuniformity) and the interface dislocation or trap density due to the presence of lattice mismatch.

Mamutin *et al* [75] employed the same wavelength dependent Raman scattering technique to reveal the defect densities of different depth in InN samples. Nevertheless, the most important wavelength dependent effect is resonant Raman scattering (RRS), i.e., when the incident photon energy approaches the actual electron transition energy (such as the band gap of semiconductors), the Raman scattering efficiency will be significantly enhanced. RRS has become more and more important especially in studying the low-dimensional superlattice, quantum well and quantum dot structures. Unfortunately, there is no study of RRS for InN so far, though that of the ternary alloy InGaN has been reported, which will be discussed in section 4.

2.7. Growth method effects

The high quality InN thin films grown by MBE [21, 22] and MOVPE [23] have been reported to have a band gap of 0.7–1.1 eV, in contrast to the previous value of 1.9–2.0 eV. It is very

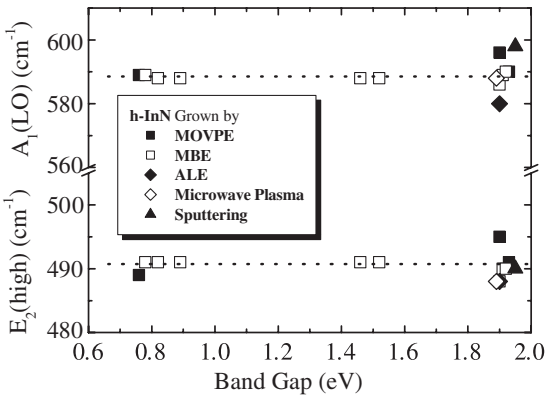

Figure 17. The Raman frequencies of E_2 (high) and A_1 (LO) as a function of reported band gaps in h-InN grown by different methods.

interesting to compare the Raman scattering structures in these InN with quite different band gaps. We notice that all the Raman modes in narrow band gap (high quality) InN can be observed in the previous large band gap InN thin films. Figure 17 summarizes the reported frequencies of E_2 (high) and A_1 (LO) modes as a function of band gap in InN grown by different methods. It is clear that the modes are also at almost the same frequencies of 491 and 589 cm^{-1}, respectively. However, fairly clear frequency differences (as large as 7 cm^{-1} for E_2 (high) and 16 cm^{-1} for A_1 (LO)) have been observed in large band gap InN mainly due to the material diversity and the disorder activation, stress and temperature effects, etc discussed above. The frequency differences in narrow band gap InN are very small (<2 cm^{-1}), and the Raman modes have narrow linewidths. These reveal the high quality and uniform InN thin films produced by modern MBE and MOVPE techniques. Saito *et al* [22] reported the narrowest linewidth of 3.7 cm^{-1} for the E_2 (high) mode in MBE grown InN at 550 °C. With the decrease of growth temperature to 460 °C, the E_2 (high) mode demonstrates a small red shift (from 491.9 to 491.1 cm^{-1}) and becomes slightly wider (from 3.7 to 4.4 cm^{-1}) due to the stress effect. Nevertheless, the PL signal decreases rapidly with the growth temperature, demonstrating the sensitivity of luminescence on InN thin film quality. This may explain the absence of luminescence in previous large band gap InN thin films before 2001, but it is still difficult to distinguish what the real band gap of InN is.

2.8. Infrared spectroscopy experiments

The even parity phonons are Raman active while the odd parity phonons are infrared active; i.e., Raman and infrared spectra are complementary in studying the lattice vibrations. In fact, both Raman and IR spectra, including transmission, reflection and ellipsometry spectra, have been employed in most lattice vibrational studies such as those of GaN [76–79]. Osamura *et al* [80] first measured long-wavelength optical phonons in polycrystalline InN film using IR reflection measurements and obtained frequencies of 478 and 694 cm^{-1} for TO and LO phonons, respectively. IR spectroscopy measurements have been employed recently for much better quality InN thin films.

IRSE has proved to be an efficient *in situ* analysis tool. When incident light polarized parallel (p) or perpendicular (s) to the incident plane reflects at the surface and interfaces of the sample, both the amplitude and the polarization status (phase) will change. The Fresnel

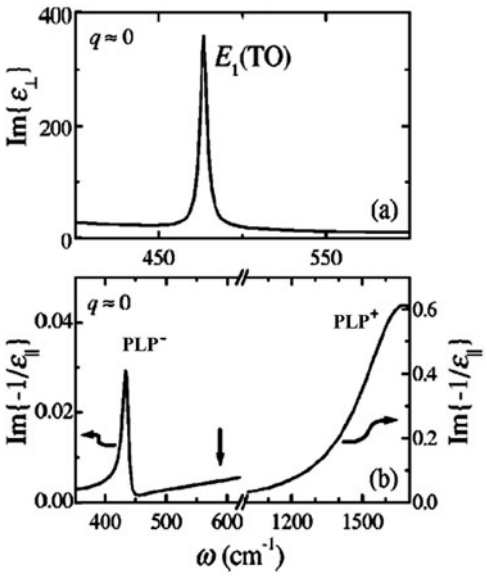

Figure 18. Dielectric constant spectra of InN obtained from IRSE. (a) $\mathrm{Im}\{\varepsilon_\perp\}$ where the E_1 (TO) structure can be observed, (b) $\mathrm{Im}\{-1/\varepsilon_\parallel\}$ where the PLP coupling structures can be observed and the frequency position marked with arrow is A_1 (LO) (from [40]).

reflection coefficient ratio can be defined as

$$\rho = R_\mathrm{p}/R_\mathrm{s} = \tan\Psi \exp(\mathrm{i}\Delta) \tag{24}$$

where Ψ, Δ are ellipsometric parameters, which represent the relative amplitude damping and phase difference of the electric vectors of E_p and E_s. Different models should be established to analyse the experimental data, especially for multilayer thin film structures. Generally, the dielectric spectrum $\varepsilon(\omega) = \varepsilon_1(\omega) + \mathrm{i}\varepsilon_2(\omega)$ is calculated from a 'vacuum/thin film/substrate' model under the assumption that the dielectric constant is homogeneously distributed. Kasic *et al* [40] studied the IRSE of InN thin film and obtained a modelling dielectric spectrum by fitting the experimental data. As figure 18 shows, the peaks of 477 cm^{-1} in $\mathrm{Im}\{\varepsilon_\perp\}$ and 435 and 1677 cm^{-1} in $\mathrm{Im}\{-1/\varepsilon_\parallel\}$ correspond to E_1 (TO) PLP mode frequencies (see the triangles in figure 8). The average effective mass of electron calculated from the dielectric function model is 0.14 m_0. Schmidtling *et al* [81] also used IRSE to estimate the influences of growth conditions on thin film quality.

The normal incident reflection spectrum based on the KK transformation is a classical way to measure the optical constants [27]. In principle, the KK transformation requires the information of the optical constant spectrum over the whole wavelength range (from 0 to ∞); however, some reasonable approximations can be made for the limited wavelength optical constant spectrum. Davydov *et al* [31] grew InN thin films with the c-axis either perpendicular to the substrate surface (sapphire (0001) plane) or parallel to the substrate surface (sapphire $(1\bar{1}02)$ plane). They analysed the IR reflection spectra at different configurations through the KK transformation and obtained the TO frequencies from the $-\mathrm{Im}(\varepsilon)$ spectrum: A_1 (TO) is 488 cm^{-1} (electric vector $E \parallel c$) and E_1 (TO) is 476 cm^{-1} (electric vector $E \perp c$). Inushima *et al* [38] obtained the wide range (0.05–6 eV) dielectric constant spectrum (see figure 19) from the IR reflection spectrum by the KK transformation. From the spectrum, the E_1 (TO) frequency is 476 cm^{-1} and the E_1 (LO) frequency is 570 cm^{-1}, determined by the extreme

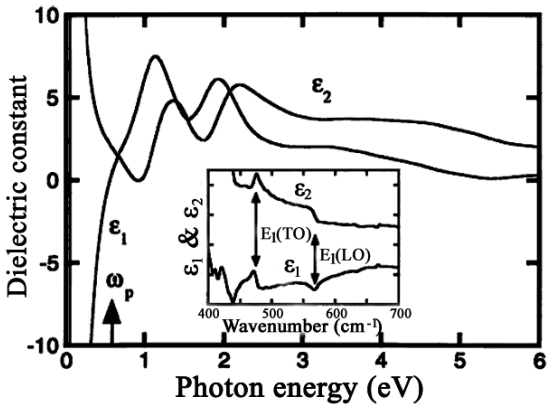

Figure 19. The dielectric constant spectra obtained from IR reflection spectra by the KK transformation. The inset shows the low frequency region, where the extreme values correspond to E_1 (TO) at 476 cm^{-1} and E_1 (LO) at 570 cm^{-1} (from [38]).

values of the dielectric constant spectrum.

Another straightforward way to analyse the IR reflection spectrum is based on the combination of a damping harmonic oscillator model and Drude model [48], which represent the contributions of TO phonons (only the TO phonon is considered because the light is transverse) and free carriers to the dielectric function $\varepsilon(\omega)$:

$$\varepsilon(\omega) = \varepsilon_\infty + \sum_i \frac{S_i \omega_{\mathrm{TO},i}^2}{\omega_{\mathrm{TO},i}^2 - \omega^2 - \mathrm{i}\omega\gamma_i'} - \frac{\varepsilon_\infty \omega_\mathrm{p}^2}{\omega^2 + \mathrm{i}\omega\gamma_\mathrm{p}} \tag{25}$$

where $\omega_{\mathrm{TO},i}$, S_i and γ_i' are the frequency, oscillator strength and damping parameter of the ith oscillator, ω_p is the plasmon frequency defined in equation (7), and γ_p is the damping constant of the plasmon:

$$\gamma_\mathrm{p} = \frac{e}{m_\mathrm{e}^* \mu} \tag{26}$$

where μ is carrier mobility, and the complex refractive index is

$$n(\omega) = \sqrt{\varepsilon(\omega)}. \tag{27}$$

In the case of normal incidence, we can get the reflection coefficient R by considering the reflections from film–vacuum and substrate–film interfaces and applying the Fresnel formula:

$$R = \left| \frac{r_\mathrm{vf} + a_\mathrm{p} r_\mathrm{fs}}{1 + a_\mathrm{p} r_\mathrm{vf} r_\mathrm{fs}} \right|^2 \tag{28}$$

where r_vf and r_fs are the reflection coefficients from vacuum to film and from film to substrate, respectively, and a_p represents the phase difference and amplitude damping between two consecutive reflections in the film. r_vf, r_fs and a_p can be expressed as

$$r_\mathrm{vf} = \frac{1 - n_\mathrm{f}}{1 + n_\mathrm{f}}, \qquad r_\mathrm{fs} = \frac{n_\mathrm{f} - n_\mathrm{s}}{n_\mathrm{f} + n_\mathrm{s}} \tag{29}$$

$$a_\mathrm{p} = \exp\left(\mathrm{i}\frac{2\omega d n_\mathrm{f}}{c_0}\right) \tag{30}$$

where d is the thin film thickness, ω is the IR radiation frequency, c_0 is the light velocity in vacuum, and n_f and n_s are complex indices for the thin film and substrate, respectively.

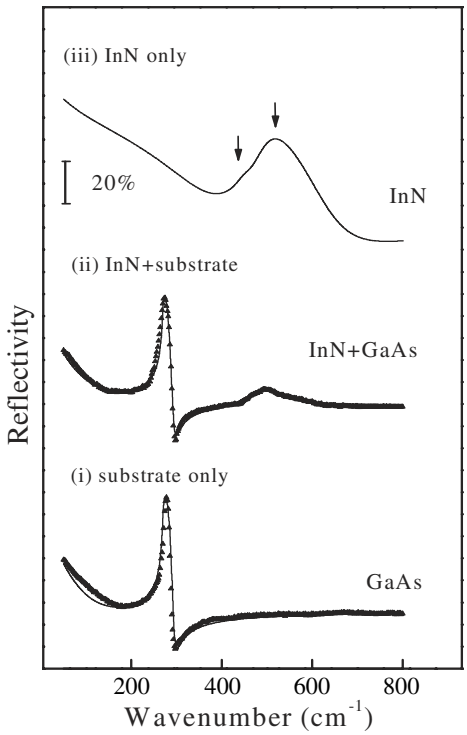

Figure 20. The fitting of IR reflection spectra of InN thin films deposited on GaAs by sputtering. The triangles are experimental data and the solid curves are calculated results (from [48]).

It should be noted that only the single component $\perp$ is considered in the above equations (25)–(30) for normal incidence. Figure 20 shows the process of fitting the IR reflection spectra by this model [48]. First, we can fit the IR reflection spectra of the GaAs substrate and get the parameters for the substrate, and then fit the spectra from thin films on GaAs substrates by equation (28) and get the parameters for the thin film (InN), through which we can calculate the reflection spectra for bulk InN. In this way, we can get not only the TO phonon parameters, but also the electric parameters such as the carrier concentration and mobility. The unexpected extra mode at 448 cm^{-1} may indeed be an indication of sample quality.

Nevertheless, the reliability of the infrared spectroscopy experiments will be influenced by some parameters, especially $\varepsilon_{\infty,\perp}$ and $m^*_\perp$ (which is anisotropic and we generally use the average value in the literature). They are taken as known parameters in the dielectric function model, but the values (calculated or experimental) have large uncertainties. For example, $\varepsilon_{\infty,\perp}$ ranges from 5.8 [38] to 8.5 [82], and different calculated values have been obtained by Persson *et al* [83] with different theoretical models. Chin *et al* [84] gave the average values of $\varepsilon_{\infty,\perp} = 8.4$ and $m^*_\perp = 0.115\ m_0$ from previously reported data. In the case of high carrier concentration, if the electric parameters can be accurately determined, we can also deduce the effective mass $m^*_\perp$ from the sharp plasma reflection edge near $\omega_{p,\perp}$ (figure 7(b) and [9]).

3. Lattice vibration of zinc blende InN

Very limited studies have been carried out for cubic zinc blende InN (c-InN) up to now, but it plays a very important role in device application, such as the excitation medium in hexagonal

(h-)InGaN based quantum well light emission devices [85]. Yamamoto *et al* [86, 87] obtained a very thin c-InN film (∼0.05 μm) on a GaAs(111) B substrate by MOVPE under a nitriding temperature below 700 °C, while a mixed phase of c-InN and h-InN was obtained on GaAs(100) substrates. Kaczmarczyk *et al* [32] and Tabata *et al* [88] reported c-InN by depositing an InAs buffer layer on GaAs(100) substrates. Recently, Bhattacharya *et al* [89] also observed c-InN on sapphire (0001) substrates grown by pulse laser deposition (PLD) from XRD and Raman scattering results.

c-InN with zinc blende structure (figure 1(b)) has a lattice constant of 4.98 Å, and a band gap of 2.2 eV. c-InN belongs to the T_d^2 space group and there are two atoms per unit cell. Its lattice vibration modes are simpler than those of h-InN: there is one LO and one TO mode at the Γ point and the optical phonons have the symmetry of $\Gamma_{15}(x, y, z)$. The Raman tensors have the following form:

$$R_{ij} = \left\{ \begin{array}{ll} \begin{bmatrix} 0 & 0 & 0 \\ 0 & 0 & \alpha \\ 0 & \alpha & 0 \end{bmatrix} & \Gamma_{15}(x) \\ \begin{bmatrix} 0 & 0 & \alpha \\ 0 & 0 & 0 \\ \alpha & 0 & 0 \end{bmatrix} & \Gamma_{15}(y) \\ \begin{bmatrix} 0 & \alpha & 0 \\ \alpha & 0 & 0 \\ 0 & 0 & 0 \end{bmatrix} & \Gamma_{15}(z). \end{array} \right. \tag{31}$$

The selection rule is also simpler; for example, at the back scattering configuration without considering the polarization, only LO can be observed from the (100) plane, only TO can be observed from the (110) plane, and both LO and TO can be observed from the (111) plane.

There have been some calculated results by different models on the phonon dispersion of c-InN [35, 90, 91]. Figure 21 shows the phonon dispersion and the DOS of c-InN [35]. Similarly to c-GaN, because of the large mass difference between the indium and nitrogen atoms, c-InN has two high peaks in the acoustic region of the DOS and flat dispersion along the Γ–X and Γ–L directions for the LO phonon. There are clear differences for the frequencies of TO and LO phonons at the Γ point obtained from different models. For example, Bechstedt *et al* [90] obtained values of 467 and 596 cm^{-1}, while Leite Alves *et al* [91] reported values of 489 and 526 cm^{-1}, respectively, in contrast to the earlier studies by Kim *et al* [67] and Wright [68], who gave calculated values of 540 and 470 cm^{-1} for the TO phonon. Since the TO phonon frequency of the cubic structure can be estimated from the A_1 (TO) and E_1 (TO) phonon frequencies of the hexagonal structure,

$$\omega_{TO} = [(\omega_{A_1}^2 + 2\omega_{E_1}^2)/3]^{1/2} \tag{32}$$

we can obtain the c-InN TO phonon frequency of 465 cm^{-1} by taking the average values of 445 and 475 cm^{-1} for A_1 (TO) and E_1 (TO) from the reported results of phonon frequencies for h-InN (see table 3). It is clear that the calculated results of Bechstedt *et al* and Wright are closer to the estimated value.

Raman scattering studies of c-InN have been reported only in [32] and [88], and the two Raman scattering results are obtained on the same sample, but with different excitation wavelengths. Figure 22 gives the Raman scattering spectra of c-InN. Tabata *et al* [88] excited the sample with a 514.5 nm (2.41 eV) laser (figure 22(a)). The two peaks located at 430 and 479 cm^{-1} were attributed to the second-order scattering of the InAs buffer layer, while those located at 457 and 588 cm^{-1} were attributed to TO and LO modes of c-InN. Kaczmarczyk *et al* [32] excited the sample with a 632.8 nm (1.96 eV) laser (figure 22(b)). The observed TO and LO frequencies were 472 and 586 cm^{-1}. We can see that the LO frequencies agree well,

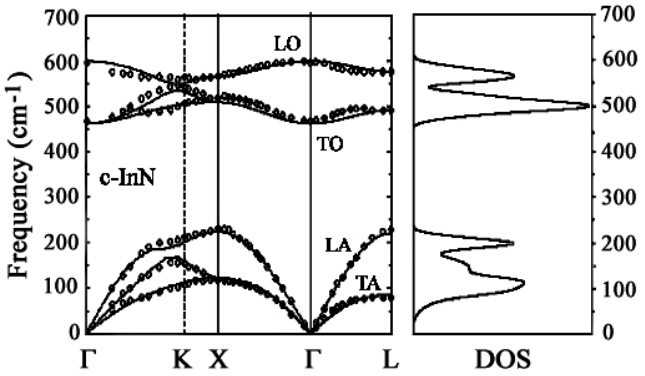

Figure 21. Phonon dispersion curves and DOS of c-InN (from [35]). The open circles are calculated values in [87].

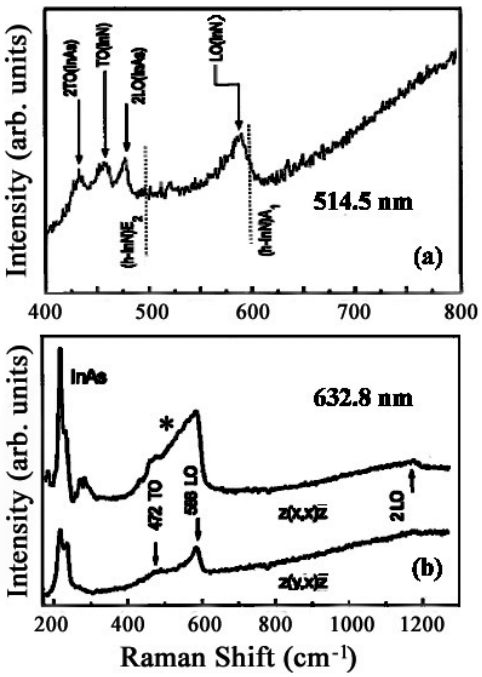

Figure 22. Raman spectra of c-InN excited by (a) 514.5 nm and (b) 632.8 nm lasers. The asterisk represents the intensification from the second-order scattering of InAs (from [32, 88]).

while the TO frequencies evidently differ. Kaczmarczyk *et al* observed that the intensity ratio between the LO of InN and TO of InAs, LO_{InN}/TO_{InAs}, was 0.36 when excited by 632.8 nm, and only 0.04 when excited by the 514.5 nm laser. They attributed this enhancement to the RRS effect, demonstrating the reliability of the first-order scattering assignment. Furthermore, the TO frequency of 472 cm^{-1} is closer to the estimated value from equation (32). The TO peak observed by Tabata *et al* may actually be second-order scattering from the InAs buffer layer.

Bhattacharya *et al* [89] confirmed the existence of c-InN by the (002) and (004) diffraction peaks in high resolution XRD, but the disorder due to the coexistence of cubic and hexagonal

phases results in a broadened band similar to the DA scattering structure (see figure 10). They attributed this band to the contributions from the DATO and DALO modes, which are located at about 492 and 572 cm^{-1}, respectively.

4. Lattice vibration of InN related alloys and low-dimensional structures

4.1. Lattice vibration in alloys

The alloys of III-nitrides have been greatly studied in recent years. For the InN related InGaN and InAlN alloys, their band gaps can be adjusted from InN (1.9–2.0 eV or 0.7–1.1 eV) to GaN (3.4 eV) or AlN (6.2 eV), which correspond to the visible–near ultraviolet band. The growth of high quality alloys is a crucial technique to fabricate related devices. There have been lots of studies on the III-nitride superlattice, quantum well and quantum dot structures and their alloys for light emission devices [92–98]. Nakamura [99] has realized a 405 nm laser diode by employing an $In_{0.2}Ga_{0.8}N/In_{0.05}Ga_{0.95}N$ multi-quantum well structure as the active region. Raman scattering can investigate many lattice and electron properties in these systems, such as the composition, uniformity, residual stress, electronic band structure and carrier concentration, and the observation of phonon properties is the fundamental work in studying these alloy systems as well as low-dimensional structures.

For $In_xGa_{1-x}N$, present phonon property studies are confined to a limited composition range due to the phase separation in the large In composition alloys [2, 100]. The phase separation is caused by the large difference between the interatomic distance of GaN and that of InN, which increases the solid miscibility gap. Although the spinodal decomposition can be suppressed by decreasing the film thickness, it will still occur when $x \geqslant 0.3$. Recently, a $In_xGa_{1-x}N$ alloy with $0.5 < x < 1$ has been successfully grown, and the PL and absorption data have also been obtained [22, 101], but no lattice vibration information.

Grille *et al* [102] calculated the phonon behaviour in mixed III-nitrides. Figure 23 shows the composition dependence of the phonon DOS at the Γ point in cubic (c-) and hexagonal (h-)InGaN and AlInN. For c-$In_xGa_{1-x}N$, both the LO and TO have one-mode behaviour. There is an impurity mode between the LO and TO, but it would not be observed in a Raman experiment due to its small spectrum intensity. For c-$Al_xIn_{1-x}N$, the LO has a one-mode behaviour while the TO has a two-mode behaviour due to the large mass difference between the Al and In atoms. There is also an impurity mode with small spectrum intensity between the two TO modes. For h-$In_xGa_{1-x}N$, both A_1 (LO) and E_2 have two-mode behaviour from the calculations (we just show the E_1 (LO) in the figure; the A_1 (LO) has a similar behaviour except for a frequency shift). But the E_2 frequency is very close to that of A_1 (TO) and E_1 (TO), which brings about a difficulty in the correct assignment of Raman scattering structures. For h-$Al_xIn_{1-x}N$, the phonon behaviour is more complex. A_1 (LO) has a one-mode behaviour, while the AlN-like E_1 (TO) and E_2 intercross with the B_1, and the E_2 mode has a weak two-mode behaviour, which is different from other alloys.

Experimental Raman scattering results of c-$In_xGa_{1-x}N$ have been reported with the composition range of $0 < x < 0.33$ [96, 103–106]. Figure 24(a) shows the Raman spectra of c-$In_xGa_{1-x}N$ with different In compositions [104]. We can see that the LO and TO frequencies decrease with the increase of the In component x, i.e., the phonon frequency shifts from that of GaN to InN. Figure 24(b) gives the linear dependence between the LO and TO frequencies and x [107], which is in good agreement with the calculation of [102], i.e., both the LO and TO have one-mode behaviour in c-$In_xGa_{1-x}N$. The 625 cm^{-1} scattering structure, as shown in figure 24(a), has been attributed to the LO mode in the separation phase of c-$In_xGa_{1-x}N$ with large x. Based on the linear relation between the frequency and the In composition, we

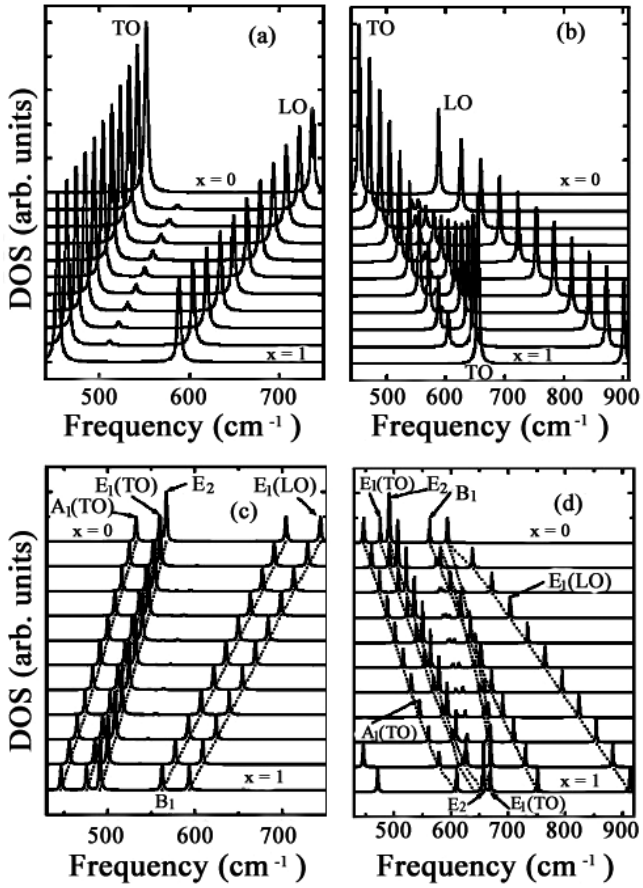

Figure 23. Composition dependent phonon behaviour at the Γ point in ternary alloys of (a) c-$In_xGa_{1-x}N$, (b) c-$Al_xIn_{1-x}N$, (c) h-$In_xGa_{1-x}N$, and (d) h-$Al_xIn_{1-x}N$ (from [102]).

can determine an x value of 0.8 (see the open circle in figure 24(b)). Silveira *et al* [105] employed the RRS technique to further study this mode. Figure 25 shows the Raman spectra of c-$In_{0.33}Ga_{0.67}N$ with different excitation energy E_L. The intensity ratio of peak S and LO (S/LO) varies with the excitation energy E_L as shown in the inset of figure 25. We can clearly observe the resonant excitation energy of about 2.4 eV, which agrees well with the PL result. An In composition of 0.72 has been estimated from the linear relation between the LO frequency and x. Furthermore, the XRD results also confirm the existence of the separation phase with an estimated x of about 0.8.

Harima *et al* [108] studied the phonon behaviour of h-$In_xGa_{1-x}N$. They found that the E_2 frequency decreases with increasing x, while no clear A_1 modes can be observed except for some scattering bands induced probably by defects (the DA modes). Due to the limited composition range ($x < 0.07$), we cannot identify that the phonon behaviour in h-$In_xGa_{1-x}N$ is either one-mode or two-mode type. Alexson *et al* [109] studied the A_1 (LO) and E_2 phonons in h-$In_xGa_{1-x}N$ with $0 < x < 0.5$ by different ultraviolet lasers. Under 325.2 nm (3.81 eV) laser excitation, both the A_1 (LO) and E_2 display sharp peaks (see figure 26(a)) since this photon energy is close to the resonant condition. But in the large x cases, the A_1 (LO) peak broadens and splits, which has been attributed to the spinodal decomposition due to the composition

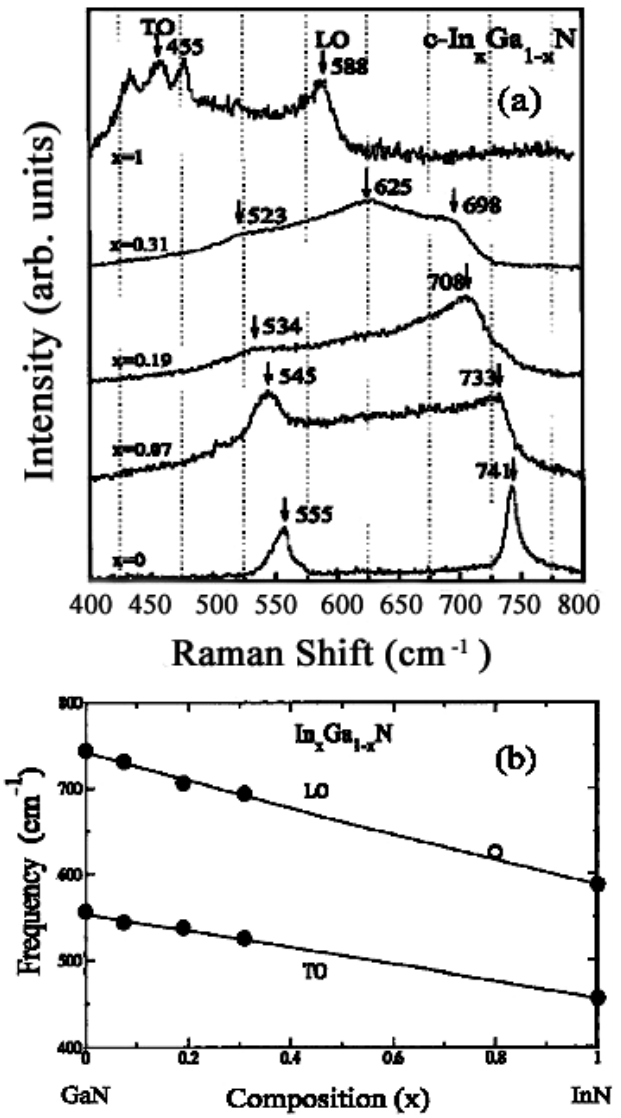

Figure 24. (a) Raman spectra of c-$In_xGa_{1-x}N$, (b) composition x dependence of the LO and TO frequencies in c-$In_xGa_{1-x}N$ (from [104, 107]).

nonuniformity. Figure 26(b) shows the x dependence of the A_1 (LO) and E_2 frequencies. The alloy A_1 (LO) frequency corresponds to that of InN when linearly extrapolating to $x = 1$, demonstrating the one-mode nature of the A_1 (LO) phonon. In contrast, the E_2 frequency has a large discrepancy with that of InN on linearly extrapolating to $x = 1$, i.e., the frequency is not simply linearly dependent on x. This result does not agree with the calculations in [102], where the E_2 is also of one-mode type. The reason may be, as we have mentioned before, that the E_2 frequency is very close to those of A_1 (TO) and E_1 (TO), which influences the determination of the E_2 peak position.

For $In_xAl_{1-x}N$, the phonon structure has been reported only by Naik *et al* [110]. They studied the Raman spectra of h-$In_xAl_{1-x}N$ with $0 \leqslant x < 0.7$ by ultraviolet and visible lasers.

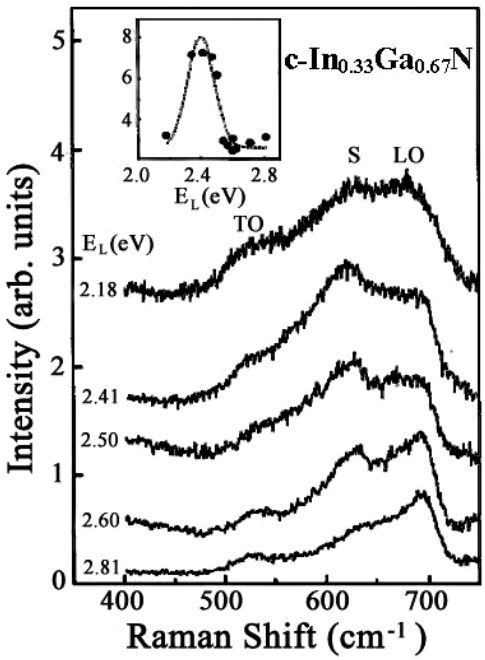

Figure 25. RRS spectra of c-$In_{0.33}Ga_{0.67}N$; E_L is the excitation energy, S is the LO phonon due to the large x separation phase. The inset shows the E_L dependence of the intensity ratio of S and LO (from [105]).

Figure 27(a) shows the Raman spectra of h-$In_xAl_{1-x}N$ ($x < 0.55$) excited by a 244 nm (5.01 eV) laser. The A_1 (LO) and two E_2 modes can be observed, and their frequencies shift to the low side when x increases. When x reaches 0.55, no evident scattering peaks can be observed due to the large difference between the band gap of the alloy (∼2.5 eV) and the excitation energy. Therefore, the samples with $x \geqslant 0.55$ are excited by a 514.5 nm (2.41 eV) laser. Furthermore, at high frequency range, two-phonon and three-phonon scattering modes (marked by arrows) are also observed. Figure 27(b) shows the relation between the frequencies of A_1 (LO) and E_2 and the Al composition $(1 - x)$, from which we can see that A_1 (LO) is one-mode type and E_2 is two-mode type in h-$In_xAl_{1-x}N$.

4.2. Lattice vibration in low-dimensional structures

The development of InN-based heterostructures and devices is in its initial stage. Growth of a suitable barrier or cap layer on InN layers is found to be difficult due to intermixing and interfusion into the InN layers. The group at Cornell University has successfully obtained an AlN barrier on InN film with evidence of two-dimensional electron gas accumulation in the InN layer, and observed very low leakage current and weak rectifying behaviour in InN-based FET structures. The recent rapid improvement in the InN film quality will result in the practical application of InN devices soon. At the present stage, lattice vibration studies on InN-based low-dimensional structures are very few because of the growth difficulties. There is only a preliminary study on InN nano-wire and some theoretical calculations, such as the interface localization of phonons in InN/GaN superlattices [111, 112]. Liang *et al* [52] obtained InN nano-wires with diameters of 40–80 nm and lengths of up to 5 μm on p type Si(100) substrates by sputtering. The A_1 (LO), A_1 (TO) and E_2 modes are observed in the Raman spectrum, but are

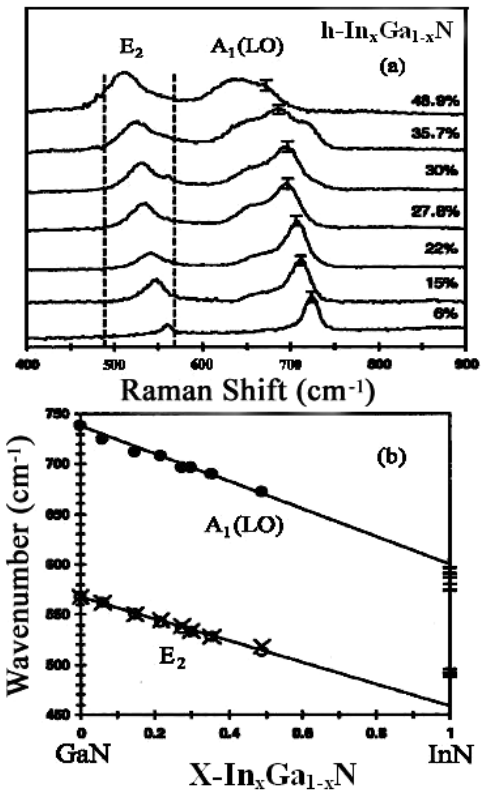

Figure 26. (a) Raman spectra of h-$In_xGa_{1-x}N$ with different indium composition x excited by a 325.2 nm laser. Dashed lines are the positions of E_2 (high) frequencies in InN and GaN. (b) x dependent A_1 (LO) and E_2 frequencies in h-$In_xGa_{1-x}N$; the small bars at the right-hand side represent the A_1 (LO) and E_2 frequencies of InN (from [109]).

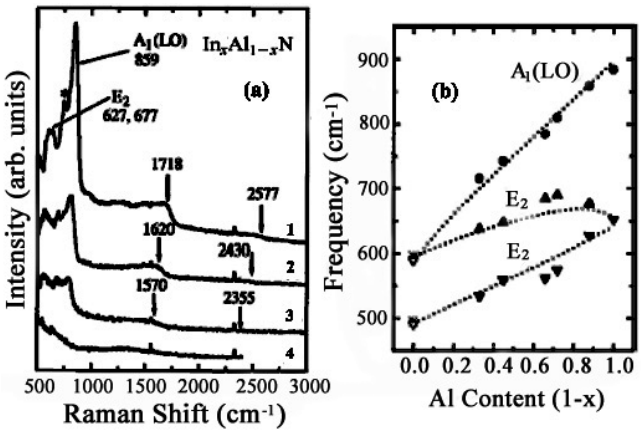

Figure 27. (a) Raman spectra of h-$In_xAl_{1-x}N$ with x of 0.12, 0.28, 0.34 and 0.55 for samples no 1, 2, 3 and 4, respectively. The structure marked with '$*$' is from the sapphire substrate. (b) Al composition $(1 - x)$ dependence of A_1 (LO) and E_2 frequencies in h-$In_xAl_{1-x}N$ (from [110]).

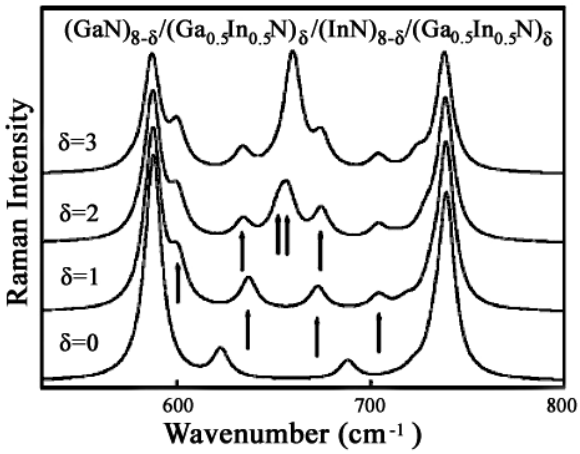

Figure 28. Calculated Raman spectra of $(InN)_{8-\delta}/(InN_{0.5}GaN_{0.5})_{\delta}/GaN_{8-\delta}/(InN_{0.5}GaN_{0.5})_{\delta}$ superlattices with interface thicknesses of different δ monolayers (from [111]).

similar to DA scattering. The Raman peaks have evident red shift, broadening and asymmetry; in particular, the A_1 (LO) mode has a red shift of 14 cm^{-1}, which can be explained by the size confinement effect in nano-structures.

Since the bonds in nitrides are more ionic, together with the large difference between the radius of cations and anions, we can predict an evident interface effect in InN/GaN superlattices due to the easy formation of a broad interface. Bezerra *et al* [111] calculated the dispersion relation and Raman spectrum of zinc blende $(InN)_{8-\delta}/(InN_{0.5}GaN_{0.5})_{\delta}/GaN_{8-\delta}/(InN_{0.5}GaN_{0.5})_{\delta}$ superlattices with interface thickness of δ monolayers. The results indicate that the interfaces have almost no effect on folded acoustic modes, but will cause a large frequency shift for confined optical modes. Figure 28 shows the calculated Raman spectra. Since the dispersion curves of the optical modes in InN and GaN do not overlap and the dispersion curves of acoustic modes are in much lower frequency region, the optical modes in ideal superlattices all belong to confined modes. The largest frequency shift caused by the interface is up to 60 cm^{-1} and some peaks will be evidently strengthened when the interface thickness δ increases. The most influenced confined mode by the interface is confined in an area of about two monolayers.

Most reported experimental results up to now have been on the InGaN/GaN low-dimensional structures. Yang *et al* [94] measured the Raman spectra of InGaN/GaN multi-quantum wells and confirmed the PL signals from InN clusters, which are formed due to the low miscibility for indium in GaN. Davydov *et al* [113] reported the Raman spectra of III-nitrides and InGaN nano-compounds. The scattering structure is a broad band between the A_1 (TO) of InN and A_1 (LO) of GaN. Wieser *et al* [114] studied the composition fluctuation in a GaN/InGaN/GaN double heterojunction by RRS and PL spectra. When the excitation frequency changes, not only does the PL peak shift, but also the LO peak shifts accordingly, which can be explained by the selective resonant excitation of the areas with different In compositions. Wagner *et al* [115] studied the strain effect in an InGaN/GaN quantum well by RRS. The A_1 (LO) frequency of h-$In_{0.13}Ga_{0.87}N$ is found to be 3 cm^{-1} lower than that of GaN and independent of excitation power density. If we only consider the composition effect (see figure 26), this frequency shift should be 10 cm^{-1} instead of 3 cm^{-1}, so the strain effect must be considered. The strain induced frequency shift is 5 cm^{-1} calculated from the

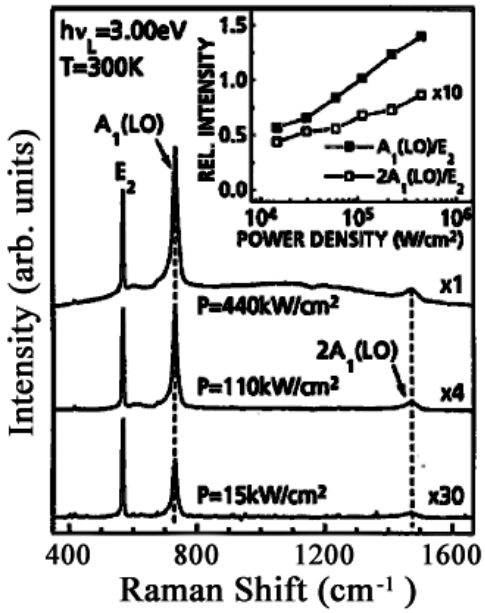

Figure 29. Room temperature RRS spectra (3.00 eV) of $In_{0.13}Ga_{0.87}N$ at different excitation power densities. The inset shows the relationship between the power density and the intensity ratios of A_1 (LO) and $2A_1$ (LO) to the nonresonant E_2 of GaN (from [115]).

deformation potential of A_1 (LO) and the estimated strain in $In_{0.13}Ga_{0.87}N$/GaN, which is close to the discrepancy of 7 cm^{-1}. Figure 29 shows that the relative intensity of the resonant excited A_1 (LO) and $2A_1$ (LO) to the E_2 of the GaN layer increases with the excitation power density. Generally, the screening effect of the piezoelectric field induced by the photo-generated carriers increases with the excitation power density, resulting in a reduction of the LO intensity. This anomaly can be explained by the fact that at low excitation power density (i.e., low carrier concentration), the piezoelectric field causes a quick separation of the electrons and holes, which broadens the exciton enhancement of the resonant Raman scattering section, while at high excitation power density (i.e., high carrier concentration), the piezoelectric field is screened and the RRS processes are recovered.

It should be emphasized that the Raman scattering studies of low-dimensional nitride semiconductors are developing rapidly and will be one of the major research interests in the future.

5. Concluding remarks

The studies of lattice vibrational properties in InN have made much progress in recent years, although these studies are not as extensive and thorough as those in GaN. For the phonon structure at the Γ point, detailed theoretical and experimental results have been reported; there have also been some limited studies on the PLP coupling, DA scattering, temperature and stress effects, and micro-Raman imaging; some theoretical and experimental results of lattice vibrations in InN related ternary alloys InGaN and InAlN have also been obtained; studies on lattice vibrations in low-dimensional structures of nitride semiconductors are becoming more and more attractive.

Very recently, Bhuiyan *et al* [116] reviewed the growth, characterization and properties of InN thin films. With the progress in growth technology, more and more confusion and problems have been proposed, and further studies are required. For example, consider the band gap of InN mentioned in the introduction; recent MBE and MOVPE grown high quality InN thin films have band gaps of 0.7–1.1 eV [21–23], which are far below the about 1.9–2.0 eV of previous (before 2002) InN. Davydov *et al* [22] attributed this to the InN–In_2O_3 compounds and InN nano-grains, due to the incorporation of oxygen impurities. In_2O_3 has a wide band gap (3.1 eV) and the quantum size effect for the nano-compounds also widens the band gap, so the absorption edge of the whole InN thin film will shift to the high energy side. Shamrell *et al* [117] proved a high concentration of oxygen impurities in sputtered InN thin films by Rutherford back scattering. From the standpoint that the larger band gap is correct, the emission at around 0.7 eV is interpreted as a deep emission. Jenkins *et al* [118] predicted deep levels near the mid-gap of InN that are responsible for an optical absorption near 1 eV. Tansley *et al* [119] identified five distinguishable defect energy levels observed in the band gap of InN. Therefore, the growth of more high quality InN film is required for further detailed studies. Nevertheless, there is not much difference in the reported lattice vibrations for these different band gap InN thin films.

Furthermore, in lattice vibration investigations, especially Raman scattering, there are still many important issues to be clarified. First, for binary InN, although the phonon structure at the Γ point is very clear, more accurate temperature dependent Raman investigations are needed to study the temperature effect; the stress effect study is limited to the E_2 mode and stress effects of other modes should be yielded; only PLP^- modes are observed for PLP coupling and n type InN has been obtained under current growth condition: the information of p type is absent; there is no information about the Raman scattering of free or bonded electrons. Second, for ternary alloys, there lacks detailed information of the phonon behaviour, especially for InGaN with large In composition and InAlN. Finally, there are very few Raman studies on low-dimensional nitride semiconductor structures, and research in this area should attract much attention in the future due to their importance in the device applications. The development of Raman spectroscopy, especially the RRS and high spatial resolution micro-Raman technique, also makes it an efficient tool for studying the phonon and electron behaviour, such as the folded modes, confined modes and free electron motions in a two-dimensional electron gas, in a nitride semiconductor superlattice, quantum well and quantum dot structures.

Acknowledgments

This work was supported in part by the National Natural Science Foundation of China (Grant No 10125416), and Shanghai municipal major basic research project 03DJ14003. The authors would like to acknowledge the discussion with Professor S C Shen at Shanghai Institute of Technical Physics, Chinese Academy of Sciences.

References

[1] Strite S and Morkoc H 1992 *J. Vac. Sci. Technol.* B **10** 1237
[2] Jain S C, Willander M, Narayan J and van Overstraeten R 2000 *J. Appl. Phys.* **87** 965
[3] Nakamura S, Senoh M, Nagahama S, Iwase N, Yamada T, Matsushita T, Kiyoku H and Sugimoto Y 1996 *Japan. J. Appl. Phys.* **35** L74
[4] Akasaki I, Sota S, Sakai H, Tanaka T, Koike M and Amano H 1996 *Electron. Lett.* **32** 1105
[5] O'Leary S K, Foutz B E, Shur M S, Bhapkar U V and Eastman L F 1998 *J. Appl. Phys.* **83** 826
[6] Starikov E, Shiktorov P, Gružinskis V, Reggiani L, Varani L, Vaissière J C and Zhao H 2002 *Physica* B **314** 171

[7] Starikov E, Shiktorov P, Gružinskis V, Reggiani L, Varani L, Vaissière J C and Zhao H 2002 *Mater. Sci. Forum* **384** 205
[8] Starikov E, Gružinskis V and Shiktorov P 2002 *Phys. Status Solidi* a **190** 287
[9] Qian Z G, Shen W Z, Ogawa H and Guo Q X 2002 *J. Appl. Phys.* **92** 3683
[10] Guo Q X, Yamamura T, Yoshida A and Itoh N 1994 *J. Appl. Phys.* **75** 4927
[11] Guo Q X, Ogawa H, Yamano H and Yoshida A 1995 *Appl. Phys. Lett.* **66** 715
[12] Guo Q X, Nishio M, Ogawa H and Yoshida A 1999 *Japan. J. Appl. Phys.* **38** L490
[13] Guo Q X, Okada A, Kidera H, Tanaka T, Nishio M and Ogawa H 2002 *J. Cryst. Growth* **237–239** 1032
[14] Aderhold J, Davydov V Yu, Fedler F, Klausing H, Mistele D, Rotter T, Semchinova O, Stemmer J and Graul J 2001 *J. Cryst. Growth* **222** 701
[15] Mamutin V, Veskin V, Davydov V, Ratnikov V, Shubina T, Inanov S, Kopev P, Karlsteen M, Soderwall U and Willander M 1999 *Phys. Status Solidi* a **176** 247
[16] Agulló-Rueda F, Mendez E E, Bojarczuk B and Guha S 2000 *Solid State Commun.* **115** 19
[17] Guo Q X, Shingai N, Nishio M and Ogawa H 1998 *J. Cryst. Growth* **189/190** 466
[18] Guo Q X, Shingai N, Mitsuishi Y, Nishio M and Ogawa H 1999 *Thin Solid Films* **343/344** 524
[19] Hwang J S, Lee C H, Yang F H, Chen K H, Hwa L G, Yang Y J and Chen L C 2001 *Mater. Chem. Phys.* **72** 290
[20] Tansley T L and Foley C P 1986 *J. Appl. Phys.* **60** 2092
[21] Inushima T, Mamutin V V, Vekshin V A, Ivanov S V, Sakon T, Motokawa M and Ohoya S 2001 *J. Cryst. Growth* **227/228** 481
[22] Davydov V Yu, Klochikhin A A, Seisyan R P, Emtsev V V, Ivanov S V, Bechstedt F, Furthmüller J, Harima H, Mudryi A V, Aderhold J, Semchinova O and Graul J 2002 *Phys. Status Solidi* b **229** R1
Saito Y, Harima H, Kurimoto E, Yamaguchi T, Teraguchi N, Suzuki A, Araki T and Nanishi Y 2002 *Phys. Status Solidi* b **234** 796
[23] Matsuoka T, Okamoto H, Nakao M, Harima H and Kurimoto E 2002 *Appl. Phys. Lett.* **81** 1246
Matsuoka T, Nakao M, Okamoto H, Harima H and Kurimoto E 2003 *Japan. J. Appl. Phys.* **42** 2288
[24] Kwon H J, Lee Y H, Miki O, Yamano H and Yoshida A 1996 *Appl. Phys. Lett.* **69** 937
[25] Harima H 2002 *J. Phys.: Condens. Matter* **14** R967
[26] Chandrasekhar D, Smith D J, Strite S, Lin M E and Morkoc H 1995 *J. Cryst. Growth* **152** 135
[27] Shen S C 2002 *Semiconductor Spectroscopy and Optical Properties* (Beijing: Scientific)
[28] Cheng G X 2001 *Raman and Brillouin Scattering—Principles and Applications* (Beijing: Scientific)
[29] Li Z F, Lu W, Ye H J, Chen Z H, Yuan X Z, Dou H F, Shen S C, Li G and Chua S J 1999 *J. Appl. Phys.* **86** 2691
[30] Matsumura S, Inushima T and Shiraishi T 1998 *J. Cryst. Growth* **189/190** 696
[31] Davydov V Yu, Emtsev V V, Goncharuk I N, Smirnov A N, Petrikov V D, Mamutin V V, Vekshin V A and Ivanov S V 1999 *Appl. Phys. Lett.* **75** 3297
[32] Kaczmarczyk G, Kaschner A, Reich S, Hoffmann A, Thomsen C, As D J, Lima A P, Schikora D, Lischka K, Averbeck R and Riechert H 2000 *Appl. Phys. Lett.* **76** 2122
[33] Bungaro C, Rapcewicz K and Berholc J 2000 *Phys. Rev.* B **61** 6720
[34] Grossner U, Furthmüller J and Bechstedt F 2000 *J. Electron. Mater.* **29** 281
[35] Tütüncü H M, Srivastava G P and Duman S 2002 *Physica* B **316/317** 190
[36] Tütüncü H M, Miotto R, Srivastava G P and Tse J S 2002 *Phys. Rev.* B **66** 115304
[37] Davydov V Yu, Klochikhin A A, Smirnov M B, Emtsev V V, Petrikov V D, Abroyan I A, Titov A I, Goncharuk I N, Smirnov A N, Mamutin V V and Inushima T 1999 *Phys. Status Solidi* b **216** 779
[38] Inushima T, Shiraishi T and Davydov V Yu 1999 *Solid State Commun.* **110** 491
[39] Dyck J S, Kim K, Limpijumnong S, Lambrecht W R L, Kash K and Angus J C 2000 *Solid State Commun.* **114** 355
[40] Kasic A, Schubert M, Satio Y, Nanishi Y and Wagner G 2002 *Phys. Rev.* B **65** 115206
[41] Abstreiter G, Cardona M and Pinczuk A 1984 *Light Scattering in Solid* vol 4 (Berlin: Springer)
[42] Gebicki W, Admowicz L, Strzeszewski J, Podsiadlo S, Szyszko T and Kamler G 2001 *Mater. Sci. Eng.* B **82** 182
[43] Parayanthal P and Pollak F H 1984 *Phys. Rev. Lett.* **52** 1822
[44] Richter H, Wang Z P and Ley L 1981 *Solid State Commun.* **39** 625
[45] Campbell I H and Fauchet P M 1986 *Solid State Commun.* **58** 739
[46] Xia H, He Y L, Wang L C, Zhang W, Liu X N, Zhang X K, Feng D and Jackson H E 1995 *J. Appl. Phys.* **78** 6705
[47] Yoshikawa M, Mori Y, Obata H, Meagawa M, Katagiri G, Ishida H and Ishitani A 1995 *Appl. Phys. Lett.* **67** 694

[48] Qian Z G, Yu G, Shen W Z, Ogawa H and Guo Q X 2002 *Physica* B **318** 180
[49] Lee M C, Lin H C, Pan Y C, Shu C K, Ou J, Chen W H and Chen W K 1998 *Appl. Phys. Lett.* **73** 2606
[50] Chen W K, Lin H C, Pan Y C, Ou J, Shu C K, Chen W H and Lee M C 1998 *Japan. J. Appl. Phys.* 1 **9A** 4870
[51] Yang F H, Hwang J S, Chen K H, Yang Y J, Lee T H, Hwa L G and Chen L C 2002 *Thin Solid Films* **405** 194
[52] Liang C H, Chen L C, Hwang J S, Chen K H, Hung Y T and Chen Y F 2002 *Appl. Phys. Lett.* **81** 22
[53] Qian Z G, Shen W Z, Ogawa H and Guo Q X 2003 *J. Appl. Phys.* **93** 2643
[54] Ingale A and Rustagi K C 1998 *Phys. Rev.* B **58** 7197
[55] Ganguli T and Ingale A 1999 *Phys. Rev.* B **60** 11618
[56] Pan Y C, Lee W H, Shu C K, Lin H C, Chiang C I, Chang H, Lin D S, Lee M C and Chen W K 1999 *Japan. J. Appl. Phys.* 1 **38** 645
[57] Bülbül M M, Smith S R P, Obradovic B, Cheng T S and Foxon C T 2000 *Eur. Phys. J.* B **14** 423
[58] Li W S, Shen Z X, Feng Z C and Chua S J 2000 *J. Appl. Phys.* **87** 3332
[59] Link A, Bitzer K, Limmer W, Sauer R, Kerchner C, Schwegler V, Kamp M, Ebling D G and Benz K W 1999 *J. Appl. Phys.* **86** 6256
[60] Liu M S, Bursill Les A, Prawer S, Nugent K W, Tong Y Z and Zhang G Y 1999 *Appl. Phys. Lett.* **74** 3125
[61] Kuball M, Hayes J M, Shi Y, Edgar J H, Prins A D, van Uden N W A and Dunstan D J 2001 *J. Cryst. Growth* **231** 391
[62] Sarua A, Kuball M and van Nostrand J E 2002 *Appl. Phys. Lett.* **81** 1426
[63] Kozawa T, Kachi T, Kano H, Nagase H, Koide N and Manabe K 1995 *J. Appl. Phys.* **77** 4389
[64] Davydov V Yu, Averkiev N S, Goncharuk I N, Nelson D K, Nikitina I P, Polkovnikov A S, Smirnov A N, Jacobson M A and Semchinova O K 1997 *J. Appl. Phys.* **82** 5097
[65] Aouas M R, Sekkal W and Zaoui A 2001 *Solid State Commun.* **120** 413
[66] Schwarz R B, Khachaturyan K and Webber E R 1997 *Appl. Phys. Lett.* **70** 1122
[67] Kim K, Lambrecht W R L and Segall B 1996 *Phys. Rev.* B **53** 16310
[68] Wright A F 1997 *J. Appl. Phys.* **86** 2833
[69] van Schilfgaarde M, Sher A and Chen A B 1997 *J. Cryst. Growth* **178** 8
[70] Krukowski S, Witek A, Adamczyk J, Jun J, Bockowski M, Grzegory I, Lucznik B, Nowak G, Wroblewski M, Presz A, Gierlotka S, Stelmach S, Palosz B, Porowski S and Zinn P 1998 *J. Phys. Chem. Solids* **59** 289
[71] Kurimoto E, Harima H, Hashimoto A and Yamamoto A 2001 *Phys. Status Solidi* b **228** 1
[72] Demangeot F, Gleize J, Frandon J, Renucci M A, Kuball M, Peyrade D, Manin-Ferlazzo L, Chen Y and Grandjean N 2002 *J. Appl. Phys.* **91** 6520
[73] Chen J, Shen W Z, Wang J B, Ogawa H and Guo Q X 2004 *J. Cryst. Growth* **262** 435
[74] Yang H F, Shen W Z, Qian Z G, Pang Q J, Ogawa H and Guo Q X 2002 *J. Appl. Phys.* **91** 9803
[75] Mamutin V V, Vekshin V A, Davydov V Yu, Ratnikov V V, Shubina T V, Ivanov S V, Kopev P S, Karlsteen M, Soderwall U and Willander M 1999 *Phys. Status Solidi* a **176** 247
[76] Giehler M, Ramsteiner M, Brandt O, Yang H and Ploog K H 1995 *Appl. Phys. Lett.* **67** 733
[77] Deguchi T and Ichiryu D 1999 *J. Appl. Phys.* **86** 1860
[78] Schubert M, Kasic A, Šik J, Einfeldt S, Hommel D, Härle V, Off J and Scholz F 2001 *Mater. Sci. Eng.* B **82** 178
[79] Kasic A, Schubert M, Kuhn B, Scholz F, Einfeldt S and Hommel D 2001 *J. Appl. Phys.* **89** 3720
[80] Osamura K, Naka S and Murakami Y 1975 *J. Appl. Phys.* **46** 3432
[81] Schmidtling T, Drago M, Pohl U W and Richter W 2003 *J. Cryst. Growth* **248** 523
[82] Bernardini F and Fiorentini V 1998 *Phys. Rev.* B **58** 15292
[83] Persson C, Ahuja R, Ferreira da Silva A and Johansson B 2001 *J. Phys.: Condens. Matter* **13** 8945
[84] Chin V W L, Tansley T L and Osotchan T 1994 *J. Appl. Phys.* **75** 7365
[85] Weintein B A, Perlin P, Christensen N E, Gorczyca I, Iota V, Suski T, Wisniewski P, Osinski M and Eliseev P G 1998 *Solid State Commun.* **106** 567
[86] Yamamoto A, Yamauchi Y, Ohkubo M and Hashimoto A 1997 *J. Cryst. Growth* **174** 641
[87] Yamamoto A, Shin-Ya T, Sugiura T and Hashimoto A 1998 *J. Cryst. Growth* **189/190** 461
[88] Tabata A, Lima A P, Teles L K, Scolfaro L M R and Leite J R 1999 *Appl. Phys. Lett.* **74** 362
[89] Bhattacharya P, Sharma T K, Singh S, Ingale A and Kukreya L M 2002 *J. Cryst. Growth* **236** 5
[90] Bechstedt F, Grossner U and Furthmüller J 2000 *Phys. Rev.* B **62** 8003
[91] Leite Alves H W, Alves J L A, Scolfaro L M R and Leite J R 2002 *Mater. Sci. Eng.* B **93** 90
[92] Wang J, Nozaki M, Lachab M, Qhalid R S, Ishikawa Y, Wang T, Naoi Y and Sakai S 1999 *J. Cryst. Growth* **200** 85
[93] Shreter Y G, Rebane Y T and Wang W N 2000 *Phys. Status Solidi* a **180** 307
[94] Yang H C, Kuo P F, Lin T Y, Chen Y F, Chen K H, Chen L C and Chyi J-I 2000 *Appl. Phys. Lett.* **76** 3712

[95] Husberg O, Khartchenko A, As D J, Vogelsang H, Frey T, Schikora D, Lischka K, Noriega O C, Tabata A and Leite J R 2001 *Appl. Phys. Lett.* **79** 1243
[96] Leite J R 2002 *Microelectron. J.* **33** 323
[97] Husberg O, Khartchenko A, Vogelsang H, As D J, Lischka K, Noriega O C, Tabata A, Scolfaro L M R and Leite J R 2002 *Physica* E **13** 1090
[98] Lischka K 2001 *J. Cryst. Growth* **231** 415
[99] Nakamura S 1998 *Gallium Nitride I* (*Semiconductors and Semimetals* vol 50) ed J I Pankove and T D Moustakas (San Diego, CA: Academic) pp 431–57
[100] Teles L K, Furthmüller J, Scolfaro L M R, Tabata A, Leite J R, Bechstedt F, Frey T, As D J and Lischka K 2002 *Physica* E **13** 1086
[101] Wu J, Walukiewicz W, Yu K M, Ager J W III, Haller E E, Lu H and Schaff W J 2002 *Appl. Phys. Lett.* **80** 4741
[102] Grille H, Schnittler Ch and Bechstedt F 2000 *Phys. Rev.* B **61** 6091
[103] Tabata A, Silveira E, Leite J R, Trentin R, Scolfaro L M R, Lemos V, Frey T, As D J, Schikora D and Lischka K 1999 *Phys. Status Solidi* b **216** 769
[104] Tabata A, Leite J R, Lima A P, Silveira E, Lemos V, Frey T, As D J, Schikora D and Lischka K 1999 *Appl. Phys. Lett.* **75** 1095
[105] Silveira E, Tabata A, Leite J R, Trentin R, Lemos V, Frey T, As D J, Schikora D and Lischka K 1999 *Appl. Phys. Lett.* **75** 3602
[106] Dutta M, Alexson D, Bergman L, Nemanich R J, Dupuis R, Kim K W, Komirenko S and Stroscio M 2001 *Physica* E **11** 277
[107] Santos A M, Silva E C F, Noriega O C, Alves H W L, Alves J L A and Leite J R 2002 *Phys. Status Solidi* b **232** 182
[108] Harima H, Kurimoto E, Sone Y, Nakashima S, Chu S, Ishida A and Fujiyasu H 1999 *Phys. Status Solidi* b **216** 785
[109] Alexson D, Bergman L, Nemanich R J, Dutta M, Stroscio M A, Parker C A, Bedair S M, EI-Masry N A and Adar F 2001 *J. Appl. Phys.* **89** 798
[110] Naik V M, Weber W H, Uy D, Haddad D, Naik R, Danylyuk Y V, Lukitsch M J, Auner G W and Rimai L 2001 *Appl. Phys. Lett.* **79** 2019
[111] Bezerra E F, Souza Filho A G, Freire V N, Mendes Filho J and Lemos V 2001 *Phys. Rev.* B **64** 201306(R)
[112] Barros E B, Lemos V, Freire V N, Gonçalves J R, Farias G A and Mendes Filho J 2002 *Phys. Status Solidi* a **194** 506
[113] Davydov V Yu, Golubev V G, Kartenko N F, Kurdyyukov D A, Pevtsov A B, Sharenkova N V, Brogueira P and Schwarz R 2000 *Nanotechnology* **11** 291
[114] Wieser N, Ambacher O, Felsl H-P, Görgens L and Stutzmanm M 1999 *Appl. Phys. Lett.* **74** 3981
[115] Wagner J, Ramakrishnan A, Obloh H and Maier M 1999 *Appl. Phys. Lett.* **74** 3863
[116] Bhuiyan A G, Hashimoto A and Yamamoto A 2003 *J. Appl. Phys.* **94** 2779
[117] Shamrell R T and Parman C 1999 *Opt. Mater.* **13** 289
[118] Jenkins D W and Dow J D 1989 *Phys. Rev.* B **39** 3317
[119] Tansley T L and Egan R J 1992 *Phys. Rev.* B **45** 10942